Check for updates

Controlling the charge state of supported nanoparticles in catalysis: lessons from model systems

Gianfranco Pacchioni [a] and Hans-Joachim Freund*[b]

Model systems are very important to identify the working principles of real catalysts, and to develop concepts that can be used in the design of new catalytic materials. In this review we report examples of the use of model systems to better understand and control the occurrence of charge transfer at the interface between supported metal nanoparticles and oxide surfaces. In the first part of this article we concentrate on the nature of the support, and on the basic difference in metal/oxide bonding going from a wide-gap non-reducible oxide material to reducible oxide semiconductors. The roles of oxide nanostructuring, bulk and surface defectiveness, and doping with hetero-atoms are also addressed, as they are all aspects that severely affect the metal/oxide interaction. Particular attention is given to the experimental measures of the occurrence of charge transfer at the metal/oxide interface. In this respect, systems based on oxide ultrathin films are particularly important as they allow the use of scanning probe spectroscopies which, often in combination with other measurements and with first principles theoretical simulations, allow full characterization of small supported nanoparticles and their charge state. In a few selected cases, a precise count of the electrons transferred between the oxide and the supported nanoparticle has been possible. Charge transfer can occur through thin, two-dimensional oxide layers also thanks to their structural flexibility. The flow of charge through the oxide film and the formation of charged adsorbates are accompanied in fact by a substantial polaronic relaxation of the film surface which can be rationalized based on electrostatic arguments. In the final part of this review the relationships between model systems and real catalysts are addressed by discussing some examples of how lessons learned from model systems have helped in rationalizing the behavior of real catalysts under working conditions.

1 Introduction

Heterogeneous catalysts, used in industrial as well as in environmental catalysis, often consist of metal nanoparticles 2–10 nm in size, stabilized on an inorganic support.[1–5] The use of metal nanoparticles is thus intrinsic to catalysis, and for this reason, has been classified as one of the first examples of nanotechnology.[6] Metal catalysts are usually prepared by wet impregnation on an oxide support, either a porous material, or a polycrystalline oxide. For a long time, it has been assumed that the oxide acts mainly as an ''inert'' support to disperse and stabilize the metal nanoparticles; according to this view, the metal is the only active species in the catalytic process. The conceptual approach has changed over the years, in particular in connection with catalysts based on very tiny metal nanoparticles,

small clusters containing up to 10 atoms, and even single metal atoms.[7] New sophisticated techniques have been developed to grow metal particles of dimensions of the order of 1 nm and below, a regime where quantum size effects[8] become dominant. Some of these materials, such as clusters of Ag and Pt, containing 3 to 10 atoms, stabilized on porous alumina have shown surprising results in terms of activity and selectivity.[9,10] More accurate characterization methods also became available, and they allowed better identification of the nature, structure and composition of a nano-catalyst, in particular under operating conditions. Transmission electron microscopy (TEM) with aberration correction[11] and *in operando* or *in situ* spectroscopy are prominent examples of those novel techniques.[12] High-resolution TEM made it possible to identify the presence of very small metal aggregates, sometimes containing just a few metal atoms on the surfaces of powder catalysts,[13] and operando spectroscopy allows for spectroscopic characterization of the catalyst during the measurement of the catalytic activity and selectivity, thus providing a closer look at structure/reactivity relationships.[14]

[a] *Dipartimento di Scienza dei Materiali, Università di Milano-Bicocca, Via R. Cozzi, 55, 20125, Milano, Italy*
[b] *Fritz-Haber-Institut der Max-Planck-Gesellschaft, Department of Chemical Physics, Faradayweg 4-6, 14195 Berlin, Germany. E-mail: freund@fhi-berlin.mpg.de*

Many studies have progressively shown that an oxide support cannot always be considered as a simple "spectator". In fact, its intimate interaction with the supported particles may result in considerable changes in the physical properties and chemical activity of the catalyst. This is particularly relevant when the particle size decreases below 1 nm. Here, the strength and nature of the interaction between the metal aggregate and the oxide support become crucial.

In some cases the chemical bonds at the metal/oxide interface are weak, and dominated by dispersion forces and polarization effects. In the majority of cases, though, new chemical bonds form due to the mixing of metal and oxide orbitals.[15] This may be accompanied by net electron transfer, with oxidation or reduction of the metal unit depending on a number of external conditions, primarily the nature of the oxide support.[16,17] The complexity of the interaction of the metal catalyst with the support reflects the complexity of an oxide surface: for instance, the same metal can behave very differently, depending on whether the interaction involves mainly the surface anions, the cations, or both.

The extreme case is that of an isolated metal atom. Take a common oxide such as TiO_2 and a gold atom (gold on titania has attracted enormous interest because of the Haruta and Hutchings discovery of the catalytic properties of nanostructured gold).[18,19] A Au atom binds weakly to the Ti^{4+} ions of the $TiO_2(110)$ rutile surface *via* polarization forces,[20] binds with a moderate Au–O chemical bond with the surface oxide anions, and gives rise to net charge transfer from the surface towards Au, which becomes negatively charged, if the interaction involves a defect center such as an oxygen vacancy.[20] Thus, a completely different behavior arises from the interaction of a metal atom (or a small cluster as well) and the various sites available on a support surface.

Of course, also the nature of the metal plays an important role. For the same stoichiometric $TiO_2(110)$ surface, while Au remains neutral and forms a covalent bond with the O anions of the surface, adsorbed Cu and Ag atoms reduce the oxide by direct electron transfer and form supported Cu^+ and Ag^+ cations,[21] thus binding to the surface *via* a completely different mechanism from that of gold.

These simple examples may illustrate the complexity of the interaction of small metal clusters with oxide surfaces. However, additional factors contributing to the overall scenario need to be considered. For instance, reducing the dimensions of the oxide support, *i.e.* generating oxide nanostructures as nanoparticles, nanowires, or thin films, may result in completely different properties of the oxide, and, hence, modify the interaction with a metal. The catalytic properties of the oxide support can also be modified *via* selective doping:[22] the presence of extrinsic defects may completely change the nature of the support, from electron-rich to electron-deficient, and can also be used to tune the properties of the supported particle. Specific examples in this direction will be illustrated in this review.

Thus, the perturbation in the electronic structure of a metal nanoparticle due to the interaction and, in particular, electron exchange with the oxide support plays a crucial role in the chemistry of the system and in the catalytic activity. To describe this kind of interaction, the term electronic metal support interaction (EMSI) was coined by Campbell.[23] This should not be confused with the classical notion of strong metal support interaction (SMSI),[24,25] an effect observed under operating conditions and consisting of the formation of an oxide layer covering the surface of the supported metal particles. SMSI and related phenomena of encapsulation often lead to a reduction, if not to the complete suppression, of the catalytic activity typically observed for the pure metal. EMSI, on the other hand, refers to the interaction of the supported metal particle with the oxide support, an effect that may lead to a change in catalytic activity, and sometimes to an enhanced catalytic activity,[26]

Gianfranco Pacchioni received his PhD at Freie Universität Berlin in 1984. He worked at the IBM Almaden Research Center, and at the Technical University of Munich. Since 2000 he has been Full Professor at the University of Milano–Bicocca where he is presently Vice Rector for Research and where he has been Director of the Department of Materials Science for several years. He has published more than 500 papers on the electronic structure of oxides and their surfaces and interfaces, defects in oxides, supported metal clusters, and catalysis. He has received several awards and is a Fellow of the Accademia Nazionale dei Lincei (2014), the Academia Europaea (2012), and the European Academy of Sciences (2009).

Gianfranco Pacchioni

Hans-Joachim Freund studied physics and chemistry at the University of Cologne where he received his PhD in 1978 and his habilitation in 1983. Between 1979 and 1981, he worked in the Physics Department at the University of Pennsylvania as a postdoctoral fellow. In 1983, he became Associate Professor at Erlangen University and in 1987 Professor at Bochum University, and in 1995, he accepted a position as scientific member and director of the Department of Chemical Physics at the Fritz-Haber-Institut der Max-Planck-Gesellschaft in Berlin. He serves as Honorary Professor of five universities. He has received several national and international awards and he is a member of several academies, scientific societies, and advisory boards of scientific journals.

Hans-Joachim Freund

This journal is © The Royal Society of Chemistry 2018

Chem. Soc. Rev., 2018, **47**, 8474–8502 | 8475

as the charge transfer at the interface can be used in principle to tune the electronic and chemical properties of the metal particle.
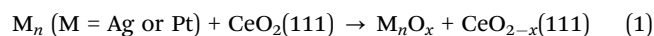
Various authors, Schwab, Solymosy, Vol'kenstein,[27–29] and others, have addressed the problem of the influence of the support on the catalyst's properties. The "Electronic Theory of Catalysis" is the conceptual framework that tries to rationalize and classify these effects.

The study of the interactions between a metal nanoparticle and an oxide support, and the control of the occurrence and direction of charge transfer have thus become central in the elucidation and rationalization of the catalytic properties of metal/oxide catalysts. Due to the efforts in the development of new preparation and characterization techniques,[30–32] often combined with accurate theoretical methods,[33] it became possible to create the premise for a deeper understanding of the problem.

The identification of charge transfer at a metal/oxide interface is not always straightforward, and may require a detailed theoretical analysis. Experimentally, a standard method applied to quantify charge transfer at metal nano-particle/oxide interfaces is X-ray photoemission spectroscopy (XPS). The proper interpretation of the spectra in terms of charge transfer is rather complex and requires distinguishing between the initial and final state effects, which depend on the particle size.[34] In particular, shifts towards high binding energies are often observed for small supported nano-particles as compared to the bulk, but are not necessarily connected to the existence of a positive charge.[35,36] Another method is electron paramagnetic resonance (EPR), which changes as the spin state of a system varies and may be used when applied to model systems or powder samples. In certain cases, where the structure of a nanoparticle is known from scanning tunneling microscopy (STM) and the various states and symmetries of the system, if present, have been determined by scanning tunneling spectroscopy (STS) (i.e. conductance imaging), it may become possible to count the number of electrons that have been transferred. There are a few case studies reported in the literature,[37–39] some of which have already been reviewed.[40] Nevertheless, some examples are included in Section 3.2 in order to illustrate the method.

As an alternative, the nature of a metal–oxide system may be studied by investigating the support instead of the metal particle. Let's take for instance the case of Ag and Pt metal particles deposited on cerium oxide, CeO_2.[41] Indirect proof that the Ag and Pt clusters are oxidized when deposited on $CeO_2(111)$ surfaces comes from the fact that the typical Ce 4f-XPS signal contains components characteristic of Ce^{3+}, indicating that some Ce ions are reduced from Ce^{4+} to Ce^{3+}. This approach has recently been used to quantify the charge transfer.[42]

Another route contributing to the reduction of an oxide surface is the so-called oxygen spillover, i.e. the diffusion of O atoms from the oxide surface to the metal nanoparticle. In the case of ceria the reaction reads as:[43]

$$M_n \ (M = Ag \ or \ Pt) + CeO_2(111) \rightarrow M_nO_x + CeO_{2-x}(111) \quad (1)$$

Density functional theory (DFT) calculations are very useful in order to disentangle the two effects. For the system considered, such calculations indicate that O spillover is energetically unfavorable on the $CeO_2(111)$ terraces (although it may be possible for the more labile oxygen atoms that reside at step or kink sites). Rather, a direct oxidation of the Ag particles occurs with the reduction of Ce^{4+} to Ce^{3+}.[44]

Having underlined the complexity inherent to the measurement of charge transfer at metal/oxide interfaces, we move now to analyze more in detail these phenomena. We start by describing the nature of the oxide support.

2 Nature of the support: oxide surfaces, nanostructuring and doping

2.1 Defect-free oxide surfaces

Inorganic oxides exhibit a wide range of properties and behaviors.[45,46] Some oxides, such as SiO_2, Al_2O_3, and ZrO_2, are wide gap insulators; others such as WO_3 and TiO_2 exhibit semiconducting behavior; some oxides belong to the special class of magnetic insulators, such as NiO and CuO, and are described by the Hubbard model and characterized by conductivity via hopping. There are also oxides with classical metallic behavior, and ReO_3 and tungsten bronzes (Na_xWO_3) are classical examples. Depending on the level of defectiveness, and on external parameters such as temperature and pressure, some oxides can undergo a non-metal to metal transition, and convert from one class to the other. Finally, there are oxides that, below a critical temperature, become superconducting.

From a chemical perspective, oxides and their surfaces[47] can be roughly classified into non-reducible oxides, where the metal cation does not easily change the oxidation state, and reducible oxides, where the metal cation can assume different oxidation states and exhibit rich redox chemistry. We will see that this distinction is quite relevant to understand the bonding mechanism with supported metals. To the first category belong simple binary oxides such as Al_2O_3, SiO_2, ZrO_2, MgO and many others; the second group is that of transition metal and rare-earth oxides (from TiO_2 to CeO_2, NiO, WO_3, etc.). The binding properties of these two groups of materials are completely different, in particular when one considers charge transfer phenomena at the metal/oxide interface. In this section we will discuss mainly SiO_2, MgO, and ZrO_2 as typical examples of non-reducible oxides, and TiO_2 and CeO_2 as representative examples of reducible oxides. The general concepts illustrated can be easily transferred to any kind of oxide.

2.1.1 Non-reducible oxides.

Binary oxides of main group elements (MgO, CaO, ZrO_2, Al_2O_3, SiO_2, etc.) are usually wide gap insulators with band gaps of 5–9 eV. The valence band consists mainly of O 2p orbitals, while the conduction band is essentially made of empty ns–np cation levels. The degree of mixing of O 2p and cation ns and np orbitals can vary substantially, with a large ionic character in some oxides (MgO, Al_2O_3, ZrO_2), and more covalent polar directional bonds in others (typical case, SiO_2). In general, these oxides have in common a top of the valence band, which is deep in energy, lying several eV below the vacuum level, and a conduction band

8476 | Chem. Soc. Rev., 2018, 47, 8474–8502

This journal is © The Royal Society of Chemistry 2018

which is quite high in energy, close to the vacuum level. This explains some general features of these materials. A deep position of the valence band implies a high cost to extract electrons from the 2p levels of the O^{2-} ions; a high position of the conduction band implies a moderate tendency to accept electronic charge. This results in low reactivity and a chemical inertness. For this reason, many of these oxides are commonly used in catalysis as "inert" supports.

These oxides are also defined as non-reducible. A quantitative measure of this property is provided by the energy cost to chemically reduce the oxide, for instance by removing oxygen from the structure. However, as we will show below, these concepts are generally valid only if one is considering a bulk oxide. Things can change radically when the oxide is nanostructured. Nanostructuring consists of producing an oxide in the form of nano-particles, nano-rods, or nano-films. The number of low-coordinated oxygen anions and metal cations changes, and increases with respect to the total of fully coordinated bulk ions. Ions at exposed sites like steps, edges, and corners[48,49] have the corresponding energies of their O 2p levels destabilized, because of a local reduction of the Madelung potential. The O 2p levels thus move up in energy, and may give rise to new states in the electronic gap of the material. The same occurs, but in the opposite direction, with the empty cation ns and np states that move down in energy with respect to the bottom of the conduction band when the coordination is decreased.[50] This has the effect to reduce the band gap of the oxide nanostructure, and to increase the tendency to donate (O sites) or accept (cation sites) electrons from the metal deposits. We will show in the following the consequences of nanostructuring by discussing the properties of the ZrO_2 bulk and nanoparticles in H_2 adsorption.

To illustrate not only some of these concepts but also the subtle problems connected with a direct measurement of charge transfer between a metal and the oxide support, we use the example of a single K atom adsorbed on alkaline-earth oxides. K is a highly reducing species, and is an ideal candidate to check (a) if electrons can be transferred to the oxide from the adsorbate and (b) the measurable consequences of this electron transfer.[51] The nature of the bonding of K with the surface of polycrystalline MgO has been studied in detail by combining EPR (Fig. 1a) with first principles DFT calculations. The experiments have shown that (a) K atoms are bound to at least three surface oxygen anions of the MgO surface (by analyzing the hyperfine coupling constants), (b) the K atoms are thermally stable up to ≈ 400 K (corresponding to a surface binding energy of ≈ 1 eV), and (c) the spin distribution of the K atom is strongly perturbed by the interaction with the substrate.[51] What the experiments cannot directly indicate is the preferred adsorption site, the reason for the high thermal stability, and, most important, the occurrence of charge transfer to or from the surface. These questions can be addressed using DFT calculations[51] which show that K atoms bind very weakly to the regular five-coordinated oxide anions (O_{5c}) of MgO terrace sites (about 0.2 eV, an energy incompatible with the observed high thermal stability). In fact, once deposited on the MgO surface, the K atoms diffuse rapidly until they become stabilized at
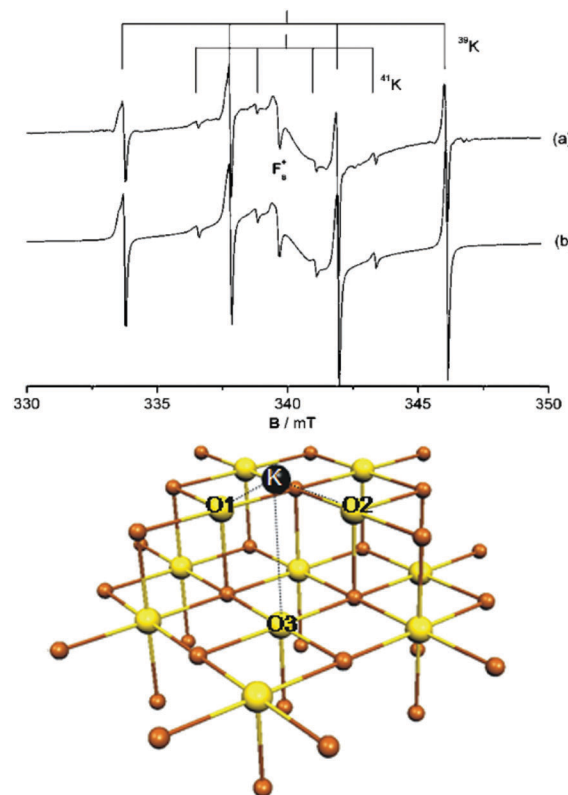

Fig. 1 Top: Experimental (a) and simulated (b) EPR spectra of K atoms deposited on MgO (spectra recorded at 77 K). Bottom: K atom adsorbed on the anionic reverse corner of the MgO surface. O atoms yellow, Mg atoms brown; O1 and O2 are O_{4c} ions, and O3 is an O_{5c} ion.[51] Reproduced with permission from ref. 51. Copyright American Chemical Society, 2005.

particular sites called reverse corners, formed by the intersection of two monoatomic steps, Fig. 1b. Here the K atom is strongly bound (by about 1 eV) and interacts with two O_{4c} ions and an O_{5c} ion of the surface. The interaction with three oxygen atoms of the surface is what has been deduced from experiments.

The stabilization of K atoms in the reverse corner sites of MgO leads to a strong polarization of the K 4s orbital. In fact, the interaction with the surface destabilizes the K 4s level. This deformation of the spin distribution results also in isotropic hyperfine coupling constants (a_{iso}) much smaller than on the free atom. Since a_{iso} directly measures the spin density at the nucleus, a simple interpretation could be that the reduction of a_{iso} reflects a partial depopulation of the K 4s orbital due to charge transfer to the oxide support. This view is incorrect. DFT calculations reproduce quantitatively the observed hyperfine interaction, but show unambiguously that a full electron resides in the valence band of the K atom. The interaction with the surface leads to a strong mixing of the spherical 4s orbital and the directional 4p orbitals, resulting in a strong reduction of the isotropic component. Thus, no charge transfer occurs, and the strong change in a_{iso}(K) has a different origin. This is an example of the added value of combining EPR measurements with DFT calculations.

The situation is similar for Li atoms adsorbed on MgO.[52] Here, due to different experimental conditions, the Li atoms are

adsorbed at low temperature and bind directly to the O_{5c} ions of the surface. The isotropic hyperfine coupling constant of a Li atom adsorbed on top of O_{5c} on the (100) terrace of MgO is $a_{iso} = 74$ G. This value is about 50% smaller than the a_{iso} value for a free Li atom (143 G in the experiment, 155 G in the calculations). Also in this case it is tempting to conclude that half an electron has been removed from the Li 2s orbital and "donated" to the surface. However, the spin density on the adsorbed Li atom is close to 1 and the large reduction in a_{iso} is due to the polarization of the Li valence electron, as for the K case described above.[51-53]

The calculations show that if a Li atom is adsorbed on reverse corner sites, where the interaction is stronger, then the a_{iso} value is further reduced to 16 G, about 1/10 of the free atom value (calculated values).[53] Once more, this could be misinterpreted, and attributed to a full ionization of the Li atom. Spin density maps obtained from DFT calculations clearly show that the electron is almost entirely localized on Li, but strongly polarized, with consequent reduction of the isotropic constant. The Li atom is virtually neutral, and no charge transfer occurs.[53]

The general message is that there is little electron transfer at the boundary between alkali metal atoms and the surface of a simple non-reducible oxide like MgO, as expected, but that a direct measurement of this from EPR is not trivial.

Of course, the picture can change dramatically in the presence of defects. If defects or dopants introduce acceptor levels in the band gap, these may lead to a spontaneous ionization of the adsorbed atoms or metal clusters, with the formation of positively charged species. Control over the concentration and nature of defects at the surface of an oxide is thus very important to determine the characteristics of the metal/oxide interface bonding and will be discussed in Section 2.2.

2.1.2 Effect of nanostructuring on the reducibility of a wide-gap oxide.

A chemical species with strong reducing properties is hydrogen. Hydrogen is widely used in catalysis to pre-treat oxide catalysts and increase their activity, directly as reacting species in hydrogenation reactions, and in many other processes. It is well known that the H_2 molecule reacts differently with non-reducible and reducible oxides. In particular, on non-reducible oxides the molecule dissociates heterolytically, with the formation of a proton, H^+, bound to an oxide anion, O^{2-} (formation of an OH group), and an hydride ion, H^-, bound to a cation (MH group). On a reducible oxide, in contrast, H_2 dissociates into two protons bound to two oxide anions (formation of two OH groups) and the corresponding electrons reduce two metal cations from M^{n+} to $M^{(n-1)+}$. Here we briefly discuss H_2 dissociation on a non-reducible oxide, ZrO_2, in order to show how nanostructuring can affect the nature of the oxide. The results are based on DFT calculations.[54]

On the regular (101) ZrO_2 surface, the H_2 molecule dissociates through a classical heterolytic mechanism, in which $Zr–H^-$ and $O–H^+$ bonds are formed. This process is slightly exothermic (-0.06 eV, Fig. 2a). The splitting through a homolytic mechanism (formation of two $O–H^+$ bonds and reduction of two Zr^{4+} centers to Zr^{3+}) is highly endothermic (1.69 eV, Fig. 2d). So, in the absence of defects, heterolytic splitting of H_2 is the only viable mechanism on the extended (101) surface, consistent with the non-reducible nature of the oxide.

Of course, a real surface can also contain morphological defects, and in particular linear steps. Ions at steps behave differently from ions at terraces, and the ZrO_2(156) stepped surface has been considered. Also in this case the splitting results in H^- and H^+ ions (heterolytic splitting). Not surprisingly, the reaction is more favorable than on the regular surface, and
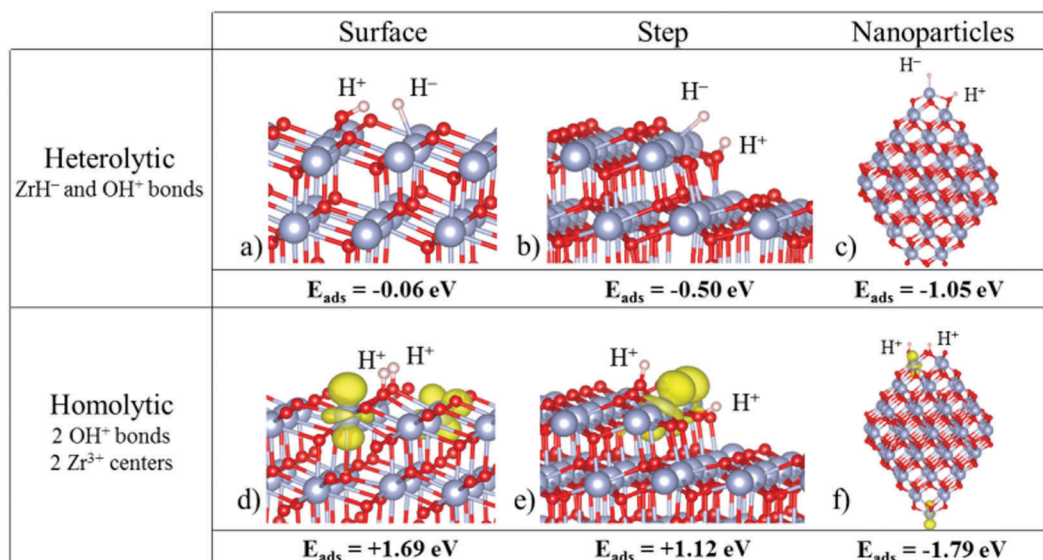

Fig. 2 Structures of hydrogen adsorbed on (a and d) the ZrO_2(101) surface, (b and e) the ZrO_2(156) stepped surface, and (c and f) a $Zr_{80}O_{160}$ nanoparticle. Top: Heterolytic dissociation; bottom: homolytic dissociation. Zr atoms are represented by big blue spheres, O atoms by small red spheres and H atoms by small grey spheres. In the homolytic mechanism, the spin density localized in reduced Zr^{3+} centers is represented in yellow ($\rho_{iso} = 0.01$ e$^-$ Å^{-3}). Reproduced with permission from ref. 54. Copyright American Chemical Society, 2016.

8478 | Chem. Soc. Rev., 2018, 47, 8474–8502

This journal is © The Royal Society of Chemistry 2018

is exothermic by -0.50 eV, Fig. 2b (the reaction energy was -0.06 eV on the regular terrace). The homolytic splitting (two H$^+$ ions and two Zr^{3+} centers) remains endothermic, by 1.12 eV, Fig. 2e, but the energy cost is considerably smaller than on the regular surface (1.69 eV). The heterolytic mechanism remains preferred also on step sites of zirconia. Stated differently, zirconia is not reduced upon simple exposure to hydrogen, as this process results in the formation of hydride ions and not in the reduction of Zr^{4+} to Zr^{3+}.

Now let us consider nanostructured zirconia, in particular in the form of stoichiometric zirconia nanoparticles of size up to 2 nm and zirconia ultrathin films deposited on Pt and Pt$_3$Zr alloys.

When H$_2$ is adsorbed on zirconia nanoparticles, a different picture is observed with respect to the regular surface. On a Zr$_{80}$O$_{160}$ nanoparticle, both H$_2$ dissociative mechanisms, heterolytic and homolytic, become exothermic, indicating a much higher reactivity of the nanoparticle compared to that of the bulk material, Fig. 2c and f. More surprising is the fact that the homolytic (reductive) dissociation process becomes the preferred mechanism (the H$_2$ dissociative adsorption energy is -1.79 eV for homolytic *vs.* -1.05 eV for heterolytic dissociation, Fig. 2c and f). This is opposite to that found for the regular terrace or the stepped surfaces. A similar behavior has been found also for smaller ZrO$_2$ nanoparticles.[54]

The opposite behavior in H$_2$ dissociation in ZrO$_2$ nanoparticles and extended surfaces is a consequence of nanostructuring, and in particular of the special electronic structure displayed by the nanoparticles.[55] This is clearly shown by a comparison of the density of states (DOS) curves for bulk, surface, stepped and nanostructured zirconia, Fig. 3. The presence of under-coordinated sites in the nanoparticles introduces low-lying acceptor states in the band gap that promote the formation of reduced Zr^{3+} centers through net charge transfer from H$_2$. Nanostructuring makes zirconia a reducible oxide, at variance with the bulk solid.
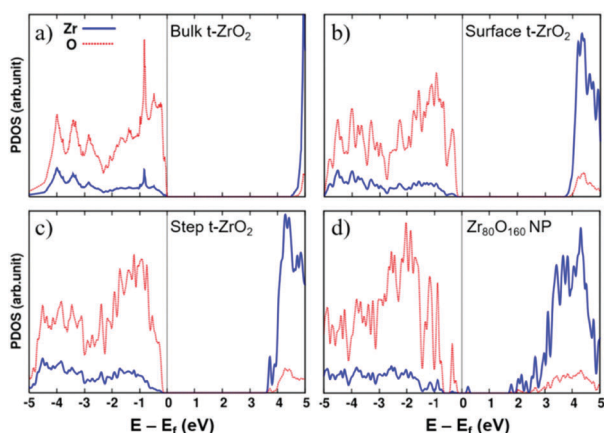

Fig. 3 Projected densities of states of (a) bulk tetragonal zirconia, t-ZrO$_2$, (b) a regular (101) t-ZrO$_2$ surface, (c) a stepped (156) t-ZrO$_2$ surface, and (d) a Zr$_{80}$O$_{160}$ nanoparticle. The zero energy corresponds to the Fermi level. Red dotted line: O contributions; blue solid line: Zr contributions. Reproduced with permission from ref. 55. Copyright American Chemical Society, 2016.

The other example of oxide nanostructures considered consists of ZrO$_2$ ultra-thin films. A two-dimensional (2D) phase of zirconia does not exist in nature. However, ZrO$_2$/Pt$_3$Zr and ZrO$_2$/Pt 2D films have been prepared and characterized experimentally.[56–62] According to DFT calculations, a free-standing, fully relaxed ZrO$_2$ 2D film is even less reactive towards hydrogen than the (101) surface.[63] In fact, H$_2$ adsorption on the relaxed 2D film is a highly endothermic process: H$_2$ dissociates heterolytically with an energy cost of $+1.55$ eV, and homolytically with an energy cost of $+3.40$ eV. This is the consequence of the lattice contraction. In fact, if H$_2$ is adsorbed on a 8.2% strained ZrO$_2$ thin film (the film is computed at the bulk lattice parameter, and subjected to considerable tensile strain), exothermic adsorption energies of -1.38 and -0.11 eV, respectively, are found for the heterolytic and homolytic dissociation mechanisms. Thus, strain in nanostructured oxide films can play a very important role in their reactivity. On unsupported ZrO$_2$ mono-layer films, the heterolytic dissociation remains preferred, as for the regular surface. Thus, zirconia becomes a reducible oxide when produced in a 1D form (nanoparticles), see above, while free-standing 2D nanostructures maintain the low reducible character typical of the bulk.[63] The reason is that the coordination of the Zr ions in the 2D film remains the same as that on the (101) surface, while a high-number of low-coordinated Zr ions are present on the nanoparticles.

A completely different picture emerges when a ZrO$_2$ 2D film is supported on Pt$_3$Zr or on Pt metals.[63] Here the films are moderately strained with respect to the bulk lattice parameter (1 to 4%). In all cases the homolytic dissociation becomes preferred. On ZrO$_2$/Pt$_3$Zr(0001), H$_2$ dissociates homolytically with an energy gain of -1.80 eV, and heterolytically with an energy cost of $+0.88$ eV. Similar results are obtained on ZrO$_2$/Pt(111).[63] With respect to the unsupported films, one notices a more exothermic H$_2$ dissociation and a preference for the homolytic mechanism. The order of stability is reversed compared to the free-standing zirconia film and the bare (101) surface.

The enhanced reactivity of the supported ZrO$_2$ thin film has two origins: (a) the lattice is slightly strained, and we have seen that strain makes the film more reactive, and (b) there is the possibility of transfer of electronic charge to the metal support. In the homolytic dissociation the charge transferred from hydrogen is delocalized partly on the metal support and partly on the oxide film, which becomes reduced. Thus, ZrO$_2$ mono-layer films supported on Pt$_3$Zr and Pt become reducible upon simple exposure to hydrogen.[63] This is due to the presence of a metal–oxide interface, more than to nanostructuring. The interface enhances the reactivity of the thin film thanks to the presence of metal acceptor states.

These results show that the concept of bulk oxide reducibility cannot be easily transferred to materials prepared in the form of very small nanoparticles or thin films, and that even oxides that are hardly reducible, and as such show a very small tendency to induce charge transfer from/to supported metals, can behave very differently under the effect of nanostructuring. In the following section we briefly discuss the general properties of classical reducible oxides.

2.1.3 Reducible oxides. By definition, reducible oxides can easily accept electronic charge from a donor species, and by

This journal is © The Royal Society of Chemistry 2018

Chem. Soc. Rev., 2018, 47, 8474–8502 | 8479

consequence, the metal cations change their formal oxidation state from M^{n+} to $M^{(n-1)+}$ by trapping excess electrons in more or less localized d or f orbitals. Transition metal (TM) and rare earth oxides belong to this category, and usually exhibit a less pronounced ionic character than simple oxides. Therefore, the O anions are not fully reduced, and have still some oxidizing power. For example, the nominal charges of TiO_2, Ti 4+ and O 2−, do not reflect the real nature of the chemical bond and the degree of ionicity. More realistic estimates indicate charges of around 2+ on Ti and 1− on O. Nevertheless, TiO_2 is formally classified as a d^0 TM compound, since its 3d states are unoccupied. By changing the stoichiometry and reducing the O : Ti ratio, the situation changes. In Ti_2O_3 Ti is in the 3+ formal oxidation state and each Ti 3d level is occupied by one electron. The very same arguments apply to CeO_2, with the only difference that the Ce 4f instead of the Ti 3d orbitals are involved.

Not surprisingly, the bonding of metal atoms and clusters with the surfaces of reducible oxides follows different rules than those for wide-gap, non-reducible oxides. First of all, the position of the top of the O 2p valence band is higher, and that of the bottom of the conduction band is lower in energy, thus leading to a higher reactivity of the material.

Of course, there are cases where metal aggregates interact with the oxide anions of reducible oxides mainly through polarization and dispersion forces, or *via* the formation of covalent chemical bonds. In this case, the bonding has similar characteristics to those found for non-reducible oxides and involves moderate electron exchange at the metal/oxide interface, due to the formation of covalent polar bonds. The metal remains essentially in a zero oxidation state, and the TM atoms do not change their oxidation state. This is the case, for instance, of Pd[64] or Pt[65] atoms and clusters adsorbed to the stoichiometric TiO_2 rutile surface: the metal atoms bind to the bridging oxygens of the surface and form strong bonds *via* hybridization of the metal d and O 2p states. However, no net charge transfer occurs.

Very different is the case of electropositive metals such as Na or K,[66–68] where the low ionization potential (IP) favors electron transfer to the supporting oxide. Taking once more TiO_2 as an example, the adsorption of Na or K on the non-defective surface results in the formation of Na^+ or K^+ ions bound to the surface oxygens; the valence electron of the alkali atom is transferred to the localized 3d states of Ti, which changes the oxidation state from 4+ to 3+.[66–68] The presence of an excess electron on the valence shell of Ti has a number of spectroscopic signatures.

Thus, while on non-reducible oxides the adsorption of potentially reducing species (alkali metals, hydrogen, *etc.*) does not lead to charge transfer, on reducible oxides there is the formation of new ionic bonds between the adsorbate and the surface, and an excess of charge accumulates on the oxide support.

Sometimes the nature of the bonding of metal nanoparticles on reducible oxides is difficult to identify and can even become a matter of controversy. Take the case of a Au atom deposited on a common oxide such as TiO_2. A classical tool to unravel the nature of the supported species is to use a probe molecule such as carbon monoxide, CO, and to measure the CO stretching frequency. If the metal atom or nanoparticle is negatively charged, the CO frequency is red-shifted due to an increased back-donation from the metal into the antibonding CO $2\pi^*$ MO; if the metal is positively charged, a blue-shift is expected. When CO is adsorbed on a Au atom deposited on TiO_2, the observed features are typical of the formation of a Au^+CO complex and a Ti^{3+} ion.[20] One could conclude that the Au atom deposited on TiO_2 is positively charged. However, DFT calculations clearly show that on stoichiometric TiO_2 a Au atom binds to the bridging oxygens with relatively weak binding, about 0.5 eV, and without charge transfer (Au remains Au^0, as shown by spin density maps that indicate the presence of an unpaired electron in the Au valence shell). The adsorption of a CO molecule, however, gives rise to a repulsion with the Au 6s orbital, and results in induced electron transfer to the oxide.[20] It is the CO probe molecule that induces the charge transfer, which is absent on the pristine material. A conceptually similar effect, but opposite in direction, has been found for CO adsorbed on a Au atom deposited on MgO.[69] Here, since the MgO support is non-reducible, there is no way to promote the Au 6s electron into accepting levels of the oxide (the MgO conduction band is too high in energy). As a result, the Au 6s electron is transferred to the CO $2\pi^*$ MO with the formation of a Au^+-CO^- complex. The presence of an excess electron on the CO $2\pi^*$ MO results in a very large red-shift of the CO stretching frequency.[69] Also in this case, however, the effect is induced by the CO molecule and is not representative of the presence of a negatively charged metal adsorbate. It should be mentioned that these effects have been observed mostly with Au atoms, and CO can be generally used as a probe molecule to check the charge nature of a metal nanoparticle supported on an oxide. However, these examples show that this technique is also not free from limitations.

Another example of controversial interpretation of data concerning the charge transfer interaction is that, already mentioned, of Ag nanoparticles deposited on CeO_2.[43,44] The analysis of the XPS spectra provides clear evidence for the reduction of the oxide by Ag deposition; in particular, the lineshape of the Ce 3d states shows the characteristic change associated with the formation of Ce^{3+} ions accompanied by a positive shift of the Ag 3d core level binding energy with respect to metallic silver. While there is no doubt about the fact that the ceria support is reduced upon silver deposition, the origin of the phenomenon is less obvious. In fact, the core level binding energies of supported metal particles are affected by final state effects arising from final state screening, which strongly depend on the size of the nanoparticles. In this respect, the simple analysis of the core level shifts of the metal nanoparticles can be misleading.[34] An attempt to disentangle the initial and final state contributions to the Ag 3d core level shifts has been done[43] based on a procedure originally suggested by Wagner.[70,71] Based on this decomposition, it was concluded that the initial state contribution to the Ag 3d core level shifts is negligible (*i.e.* the observed positive shift is entirely due to final state screening), and that the Ag nanoparticles on $CeO_2(111)$ are metallic (zero oxidation state).[43]

This conclusion contrasts with the results obtained from DFT calculations which show a tendency of the Ag nanoparticles to

become oxidized by simple contact with the ceria surface (formation of Ce^{3+}).[44] In order to rationalize the apparent reduction of ceria, it has been suggested that the spillover of lattice oxygen occurs at the Ag/CeO_2 boundary, and that oxygen diffuses on the surfaces of the Ag nanoparticles, thus leading to a CeO_{2-x}/Ag_nO_m system, see eqn (1). However, thermodynamic data suggest that the transfer of oxygen from the ceria support to Ag particles is thermodynamically unfavorable. Further evidence in favor of direct charge transfer comes from STM measurements since a direct increase of the concentration of Ce^{3+} ions with the amount of Ag deposited has been observed.[44]

This brief discussion well illustrates the complexity of the interaction of metal nanoparticles with the surfaces of reducible oxides. In particular, the reduction of the oxide can originate from direct electron transfer or from the oxygen reverse spillover mechanisms. Clearly, the experimental conditions are very important to define which mechanism is dominating.

There are cases where not only the occurrence of charge transfer can be unambiguously proven, but also the amount of charge transferred can be quantified. We shall briefly review examples, where this has been pioneered for thin films in the next section.[37,39] In the present example Pt^{72} atoms and clusters deposited on the regular $CeO_2(111)$ surface may become substantially oxidized with the formation of positive charges on the metal side and reduced Ce^{3+} ions on the support. In a combined DFT and photoelectron spectroscopy study, the origin and nature of metal–oxide interactions on well-defined Pt–ceria catalysts have been elucidated.[42] The method used is resonant photoemission spectroscopy at photon energies that lead to resonant enhancement of features associated with either Ce^{3+} or Ce^{4+}. From these resonant enhancements it has been possible to derive the surface concentration of Ce^{3+} ions by calibration with conventional XPS and, therefore, count the number of electrons that are transferred between the Pt particles and the ceria support.

Three important quantities have been monitored as a function of particle size, Fig. 4:[42] the number of electrons transferred per Pt particle, the number of electrons transferred per Pt atom and the number of electrons transferred per surface area. The number of electrons transferred per particle increases linearly with size for particles with up to 70 Pt atoms. For larger particles further charge transfer is suppressed. Interestingly, the charge per Pt atom shows a maximum at particle sizes between 30 and 70 Pt atoms (1–1.5 nm). Here, it reaches a peak value of about 0.11 electron per Pt atom. This means that the Pt nanoparticles become partially oxidized, forming $Pt^{\delta+}$ with an average charge of $\delta \sim 0.11$. The maximum charge transfer per surface area amounts to 1.2×10^{18} electrons m^{-2}, which corresponds to about 17% of the surface cerium ions being reduced to Ce^{3+} (on average one out of six Ce^{4+} surface ions is reduced to Ce^{3+}).

Interesting, for smaller Pt particles, nucleation occurs at defects and hinders the charge transfer from Pt to ceria. This opens the topic of defective oxide surfaces that will be addressed in the next section. In general, the results reported in ref. 42 show that the charge transfer can be tuned by adjusting the
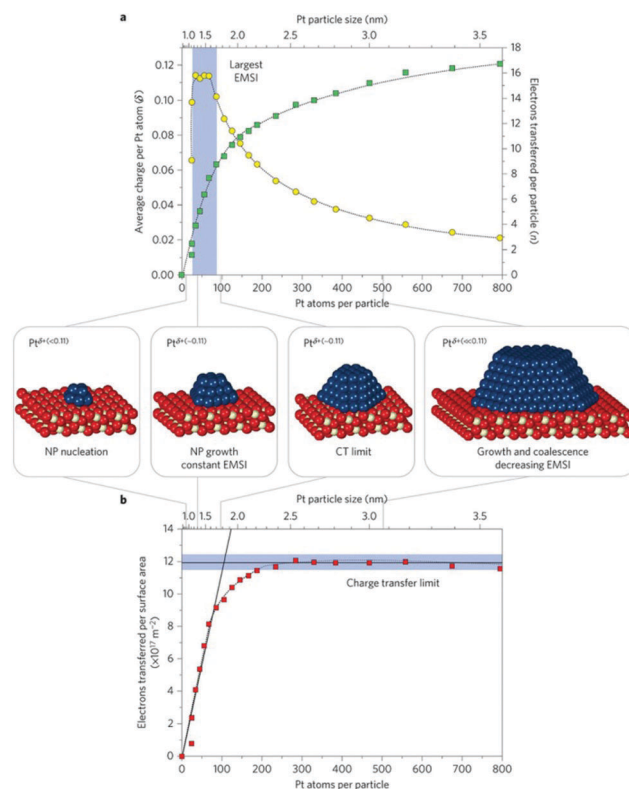

Fig. 4 (a) Number of electrons transferred per Pt particle to the ceria support as a function of particle size (green squares). The partial charge per Pt atom reaches a maximum for particles with 30 to 70 atoms (yellow circles). (b) At higher Pt coverage the total amount of transferred charge approaches a limit (charge transfer limit, red squares). The atomic models show schematically the average particle sizes in the different regions. Reproduced with permission from ref. 42. Copyright Springer Nature, 2016.

particle size, the particle structure and the chemical properties of the support.

2.1.4 Hydrogen on and in reducible oxides. Recently, it has been observed that fully oxidized CeO_2 nano-particles unexpectedly hydrogenate triple carbon–carbon selectively to carbon–carbon double bonds.[73,74] The mechanism for this interesting observation is completely unclear. In this connection model studies are of key importance. A question to be answered is how the hydrogen on or in ceria is involved in the reaction. This means that we need to define a ceria surface and apply analytical techniques that allow us to differentiate hydrogen on the surface and in the bulk of the material.[75,76] We have used resonant-nuclear reaction analysis to show that there is both hydrogen on the surface, additionally identified using IRAS as OH groups, and in the bulk of the material. This can only be done on well-defined model systems. It will provide essential information as input to understand the real catalyst's chemistry.

2.2 Defective oxide surfaces

2.2.1 Intrinsic defects. Defects play a very important role in the chemistry of oxide surfaces.[77] The are various kinds of point defects that can be found on an oxide surface: low-coordinated

This journal is © The Royal Society of Chemistry 2018

Chem. Soc. Rev., 2018, 47, 8474–8502 | 8481

cations and anions,[48] isolated cation[78] and anion vacancies,[79–82] aggregated ensembles of vacancies,[83] hydroxyl groups,[84] peroxo groups,[85] grain boundaries, *etc.* Of course, the effect of the defects on the material properties is directly proportional to their concentration: completely different situations arise when the concentration of defects is low, typically below 10^{-6}–10^{-7} defect sites per mole, or when it is large, of the order of 10^{-2}–10^{-3}. At high concentrations of cation or anion vacancies, it is more appropriate to refer to the system as non-stoichiometric. Non-stoichiometric oxides exhibit electronic properties completely different from those of the stoichiometric phases.[86]

From a general point of view, a defect is an irregularity in the crystal lattice. Due to its structural characteristics, it is associated with new electronic states; often these states appear in the gap of the insulating or semiconducting oxide. One can distinguish two general cases. (1) Defects that introduce new acceptor levels below the conduction band of the material; these levels can act as good electron acceptors, and can contribute to the ionization (or partial oxidation) of deposited metal atoms and clusters. On non-reducible oxides these defect centers can play the same role of the d and f orbitals of TM atoms in reducible oxides: they can trap excess electrons, and favor the charge transfer from a metal nanoparticle to the oxide. Of course, the number of defect centers is orders of magnitude smaller than the number of cations in reducible oxides. (2) In the second scenario, defects introduce new occupied donor levels, sufficiently high in the band gap to lie above the empty (accepting) levels of the adsorbed metal species; when this occurs, electrons can be transferred from the defect to the metal particle. This is often the case when neutral oxygen vacancies are present. Notice that, in order for this charge transfer to occur, it is not necessary that the defect lies on the surface of the material. Sub-surface and even bulk defects may generate donor states in the gap, and the corresponding electrons can be donated to a deposited metal nanoparticle, provided that there is sufficiently high electron mobility.

We illustrate these cases by considering two specific examples. The first one is again the deposition of Na or K atoms or clusters on the surface of a non-reducible oxide, but now in the presence of specific defects able to trap electrons. We have seen above that on the non-defective surface of a simple oxide (*e.g.* MgO), a K atom (or cluster) is bound by polarization effects with virtually no charge transfer.[51,87] In contrast, on-defect rich MgO surfaces a spontaneous ionization of the alkali metal may occur, with a behavior that is reminiscent of that of reducible oxides. This is the case, for instance, of the hydroxyl group (OH).[88] Hydroxyls are always present on the surface of an oxide, as they result from the dissociative adsorption of water.[89] For reactions occurring at room temperature or slightly above, the oxide surface is partly hydroxylated, and the surface reactivity can be significantly modified compared to a fully dehydroxylated case. Here we discuss cases where OH groups are present in low amounts, and as such can be classified as defects.

The electron trapping ability of OH groups has been demonstrated using EPR by adsorbing Na atoms on fully dehydroxylated and on partly hydroxylated MgO surfaces.[88] A MgO polycrystalline
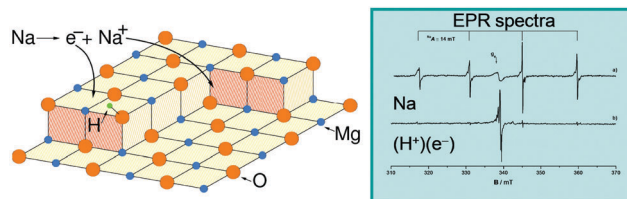

Fig. 5 Left: Schematic representation of the interaction of a Na atom with an hydroxylated MgO surface. The Na atom dissociates into a Na$^+$ ion stabilized at a reverse corner and an electron trapped near an OH group of the surface where it forms a (H$^+$)(e$^-$) center. Right: EPR spectra of Na atoms deposited on a fully dehydroxylated MgO surface (top) and on a partly hydroxylated MgO surface (bottom).[93] Reproduced with permission from ref. 93. Copyright American Chemical Society, 2007.

sample has been exposed to low doses of Na vapor; Na atoms adsorb on the surface and give rise to an EPR signal, which indicates the presence of an unpaired electron in the Na 3s orbital (Na remains neutral and no CT occurs), Fig. 5. The experiment has been repeated on a partly hydroxylated MgO sample. Surprisingly, the EPR spectrum assumes a completely different shape, and exhibits a line shape that has been unambiguously assigned to electrons trapped near OH groups. What occurs is that Na adsorption is followed by the ionization of the Na atoms (formation of Na$^+$ bound to oxide anions), with the valence electron of Na stabilized at a trapping site formed by a low-coordinated Mg^{2+} ion and an OH group. In a similar way, also H atoms interacting with the MgO surface can split to form a proton, H$^+$, bound to an O^{2-} ion (formation of an OH$^-$ group), and an electron stabilized by the local electrostatic potential near the OH group;[90,91] these centers have been named (H$^+$)(e$^-$) centers.[92] These experiments show that by simple hydroxylation the chemistry of the MgO surface changes drastically, leading to a spontaneous ionization of Na atoms and clusters, which is not observed on the hydroxyl-free surface.

Other defects, which are able to ionize adsorbed metal species, are cation vacancies, low-coordinated cation sites, and grain boundaries. Electronic structure calculations have shown that grain boundaries at MgO nanocrystals can trap electrons and generate states just below the conduction band, Fig. 6a and b;[94] experimental studies on the deposition of Au clusters on MgO/Mo(100) films have shown a tendency for the nanoparticles to nucleate along the dislocations and grain boundaries, Fig. 6c.[95] Of course, if excess electrons accumulate at grain boundaries, they can also be transferred to deposited metal nanoparticles. STM experiments have shown the presence of an excess of charge on the supported Au clusters due to their interaction with extended defects.[95]

The most studied defect center with an ability to transfer electrons to supported metal atoms or nanoparticles is the oxygen vacancy.[96] The nature of oxygen vacancies varies a lot from oxide to oxide, but it has in common that the removal of a neutral oxygen leaves behind an electron rich surface. The way these excess electrons are distributed in the solid varies substantially with the nature of the oxide. In ionic oxides such as MgO, CaO, ZrO$_2$, *etc.*, two electrons are trapped at the site created by the missing O atom and stabilized by the strong

8482 | *Chem. Soc. Rev.*, 2018, **47**, 8474–8502

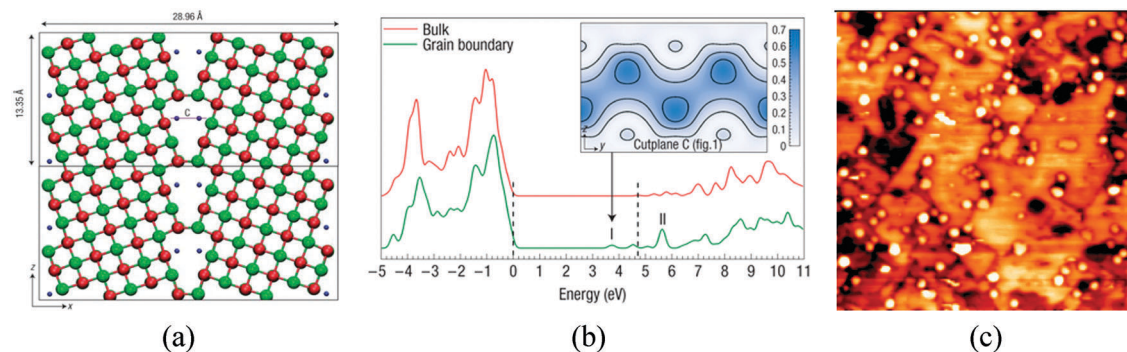This journal is © The Royal Society of Chemistry 2018

Fig. 6 (a) Electrons trapped inside a dislocation in MgO nanocrystals (blue points); and (b) DOS for bulk MgO and MgO grain boundaries with trapped electrons. The dashed lines indicate the positions of the bulk valance-band maximum and conduction-band minimum. I and II label the electronic states associated with the grain boundary. The inset shows electron density isosurfaces for an electron in state I.[94] Reproduced with permission from ref. 94. Copyright Nature, 2008. (c) STM topographic image of Au clusters deposited on a 12 ML thick, electron-bombarded MgO/Mo(001) film (100 × 100 nm^2). The aggregates preferentially nucleate at the dislocation lines in the film.[95] Reproduced with permission from ref. 95. Copyright American Chemical Society, 2010.

Madelung field.[96,97] In SiO$_2$, a solid characterized by covalent polar $\equiv$Si–O–Si$\equiv$ bonds, the removal of an O atom results in the formation of a direct $\equiv$Si–Si$\equiv$ two-center, two-electron, bond, with considerable relaxation of the lattice following oxygen removal.[98] In reducible oxides, the electrons associated with the missing O atom are transferred to the empty d or f levels of the M cation (the 3d states of Ti in TiO$_2$[99] or the 4f states of Ce in CeO$_2$),[100,101] with a consequent change in the oxidation state, from M^{4+} to M^{3+}. This localization leads to a local distortion due to the formation of a small polaron.

The presence of O vacancies on the surface (or sub-surface) of the oxide may result in major modifications of the interaction with deposited metals.[102,103] This effect has been not only predicted by several theoretical calculations, but also demonstrated experimentally by non-contact AFM, Fig. 7.[104] In particular, the forces acting between the metal tip (a PtIr alloy) and the regular oxide anions or oxygen vacancies of a MgO(100) surface have been measured. The presence of vacancies on the surface has been proven by use of an STM tip, and the local forces between the tip and the defect have been measured and compared with the forces between the tip and the regular sites. The interaction energy of the tip is about three times larger with the defect center than with the regular sites. Furthermore, the tip–vacancy interaction acts at relatively long distance from the defect (>5 Å), suggesting that atoms or clusters diffusing on a surface may experience the attractive potential of the defect when they are on its proximity and can then be trapped at the defect center.[104] Nucleation and growth start at these specific sites.

Normally, when metal atoms or clusters interact with anion vacancies, charge transfer occurs from the support to the adsorbed metal. The occupied levels of the defect lie high in the gap, and they can be above the Fermi level of the deposited metal particle, inducing electron flow. There is a vast literature on the consequences of this interaction. One measurable effect of the charge transfer is the shift in the vibrational frequency of CO molecules adsorbed on the metal particle. Due to the excess charge accumulated on the metal unit, and the consequent

reinforcement of the back-donation mechanism, the CO stretching frequency shifts to the red by about 50 cm^{-1} for a particle of 1–2 nm diameter,[105] as shown for Au nanoparticles deposited on MgO thin films where oxygen vacancies have been created on purpose by electron bombardment.[106]

The same effect occurs for metal atoms or clusters deposited on reduced TiO$_{2-x}$ or CeO$_{2-x}$ surfaces. Also in this case the defect states (Ti 3d or Ce 4f) lie at relatively high energy in the gap (about 1 eV below the CB in TiO$_{2-x}$[99] and about 2 eV below the 5d band in CeO$_{2-x}$).[107,108] Metals with high work functions promote electron transfer from the defect centers. Since the mobility of trapped electrons in semiconducting oxides is relatively high (the computed barriers for diffusion for TiO$_2$ are of the order of 0.2 eV),[109] the nanoparticle does not need to be in direct contact with the vacancy in order to become charged. This effect has been used to design more efficient photo-catalysts where a semiconducting oxide such as TiO$_2$ is interfaced with Au nanoparticles which can act as electron scavengers and reduce the electron–hole recombination, with direct improvement of the photocatalytic activity.[110]

Of course, the occurrence of charge transfer when a cluster or a nanoparticle is deposited on or near O vacancies depends on the nature of the metal. For instance, in a combined STM and DFT study of Pt and Au monomers, dimers, and trimers deposited on a regular and defective TiO$_2$(101) surface,[111] it has been shown that while the Au clusters become negatively charged when deposited on the O vacancies, Pt clusters do not show an appreciable change in their charge state.

2.2.2 Extrinsic defects. The chemical properties of a supporting oxide can be modified, to some extent in a controlled way, *via* doping with external atoms.[22] Doping of oxides is a very broad topic, with direct implications also on catalysis, and as such is subjected to a large number of studies. One can replace cations or anions in the lattice of an oxide material with external atoms; impurity atoms can enter in the structure also as interstitial species, and, not surprisingly, things are quite different depending on the nature of the dopant, substitutional or interstitial. Often, the substitution of a lattice ion with a new
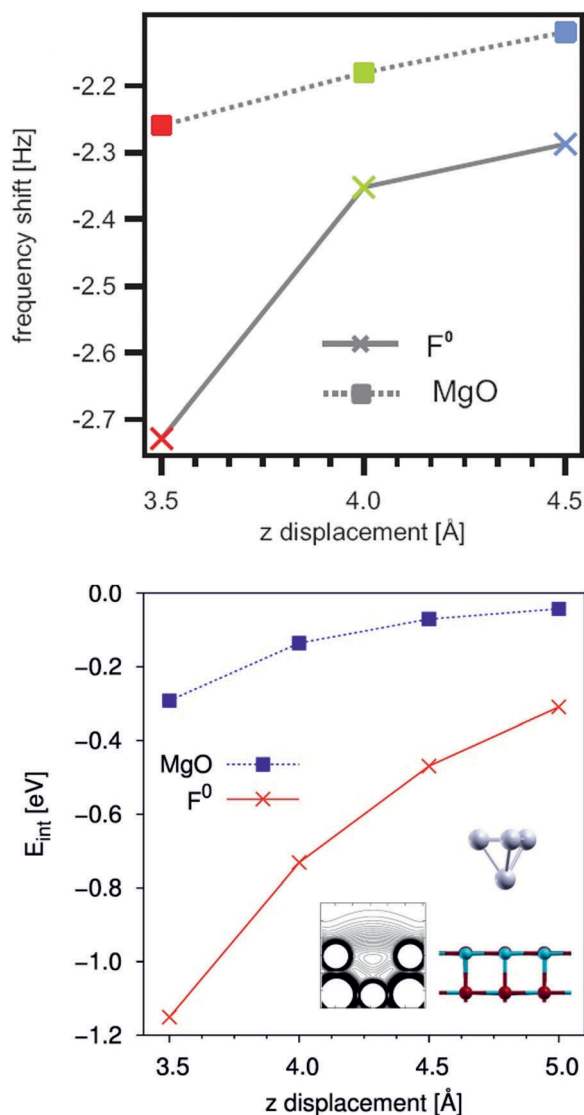
Fig. 7 (Top) Resonance frequency shift of a $Pt_{0.9}/Ir_{0.1}$ STM tip on a regular MgO surface (rectangles) and above an oxygen vacancy (F^0) defect site (crosses). The resonance frequency shift is a direct consequence resulting from potential gradients between the tip and the sample. (Bottom) Interaction energy of a Pt_4 cluster above the O site of a MgO surface (rectangles) and above a F^0 defect center (crosses) calculated by DFT.[104] Reproduced with permission from ref. 104. Copyright American Chemical Society, 2010.

element with a different valence results in an excess or in a lack of charge, leading to a charge imbalance in the system. In order to maintain electro-neutrality, other defects may be generated that compensate for this charge imbalance. The number of possible mechanisms to compensate for the charge imbalance is quite large, and involves the creation of other defects and irregularities in the crystal. A discussion of the various possibilities goes beyond the scope of this review. Here we briefly discuss some basic concepts and examples that can be used to design new materials in order to promote charge transfer to or from supported metal nanoparticles, and generate in this way new catalysts with tailored properties.[112,113]

An oxide can be doped with an element whose valence is lower than that of the replaced cation (*e.g.*, trivalent La replacing tetravalent Ce to form $La_xCe_{1-x}O_2$);[112] such materials are known as "low valence dopants". These dopants create an "electron deficit", and one consequence is that the oxygen atoms around the defect have their charge decreased, and therefore bind more weakly to the doped oxide than to the undoped one. The net effect of the low-valent dopants is to make the oxide more reactive in oxidation reactions than the undoped one. According to DFT calculations[22] the effect takes place for all oxides and for all low-valent dopants. If doping results in less strongly bound O atoms on the surface, it also favors the formation of O vacancies.

The opposite case is that of a "high-valent dopant", which replaces a metal cation in the oxide. A typical case is a trivalent Al that replaces a divalent Mg in MgO. Al enters as Al^{3+} in the crystal when it replaces a Mg^{2+} ion, and its extra valence electron is transferred to the rest of the lattice. In the absence of defects, the excess electron provided by the Al dopant can only occupy the conduction band of the material, and become delocalized over a large number of Mg ions of the surface.[114] This is a rather unlikely process, because the conduction band of MgO is very high in energy and the oxide is non-reducible. However, morphological irregularities or point defects are always present, and have electronic states below the bottom of the conduction band where the excess electron coming from the dopant can be trapped and localized. The oxide becomes rich in excess electrons which can be transferred to an adsorbed metal catalyst if the proper level alignment is achieved.

Similar effects occur by doping simple oxides like MgO or CaO with TM atoms. An example is that of Mo dopants on the growth of gold on a CaO(001) surface (this will be further discussed below, see Section 4.1).[115] Mo-doped CaO (CaO_{Mo} where about 2% of Mg ions are replaced by Mo) and undoped CaO films have been prepared and their adsorption properties have been studied. By growing a few layers of pure CaO on top of the doped sample, segregation of Mo dopants to the surface has been avoided. In this way, no direct interaction between the Au deposits and the Mo dopants is possible. Deposition of Au at 300 K on pure CaO films results in the formation of 3D gold particles, indicating that gold follows a Volmer–Weber growth, typical of weak adhesion and small or no charge transfer between the metal and the oxide support.[116,117] In contrast, on the doped CaO_{Mo} films Au forms 2D islands of monolayer height, Fig. 8. This growth mode of Au clusters is typical of strong metal/oxide interactions dominated by charge transfer from the support to gold, and has been demonstrated for Au aggregates on MgO/Ag(100) ultrathin films (see below, Section 3.2).[118,119] DFT calculations have shown that Mo^{2+} ($4d^4$) is an intrinsically unstable species that tends to donate charge to accepting species forming more stable Mo^{3+} ($4d^3$) or Mo^{4+} ($4d^2$) cations. The presence of Mo dopants introduces high-lying donor states that efficiently transfer charge to a metal with high electron affinity, such as Au. Thus, doping CaO with Mo results in charge transfer from the doped oxide to the Au particle, at variance with the pure oxide.
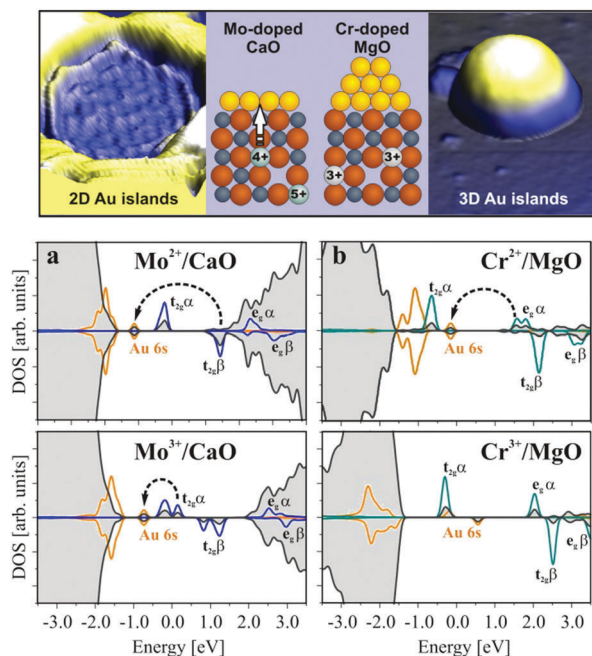
8484 | *Chem. Soc. Rev.*, 2018, **47**, 8474–8502

This journal is © The Royal Society of Chemistry 2018

Fig. 8 Top: STM topographic images of Mo-doped and Cr-doped MgO(001) films. Bottom: Projected densities of states (DOS) for (a) CaO_{Mo} and (b) MgO_{Cr} in the presence of a Au atom calculated for two different charge states of the transition metal ion. Charge-transfer processes from the HOMO of the dopant to the Au 6s affinity levels are indicated by arrows.[120] Reproduced with permission from ref. 120. Copyright American Chemical Society, 2012.

One should not conclude that every TM dopant behaves in the same way. The final effect depends on the chemical nature of the dopant. For instance, doping MgO with Cr does not lead to any appreciable difference in adsorption properties compared to the pure MgO surface, Fig. 8.[120] In both cases, there is no effect of the Cr dopant on the donor properties of the oxide and charge transfer does not occur. The reason for the different behaviors of MgO_{Cr} and CaO_{Mo} is that while the Mo ion in CaO_{Mo} results in excess electrons on the oxide, in MgO_{Cr}, Cr^{3+} species replace Mg^{2+}, leading to the formation of cation vacancies in order to maintain electroneutrality (see above). The occupied Cr^{3+} states are below or at a similar energy of the Fermi level of Au clusters, which renders electron transfer unfavorable, Fig. 8.[120]

3 Oxide ultrathin films as model systems

3.1 Preparation

Ultrathin films of insulating materials are attracting increasing interest thanks to their uncommon physico-chemical properties. The field has grown very rapidly after the discovery of materials in the form of single layers. Graphene is the prototype of two-dimensional materials, but several other examples are known.[121] Two-dimensional materials have been studied intensively for a variety of potential applications.[122,123] Thin layers of oxide materials, however, have been used in various technologies in the last few decades. For instance, ultrathin silicon dioxide films have been the basis of metal oxide field effect transistors;[124] to a large extent the microelectronic revolution is based on the excellent properties of thin SiO_2 films grown on silicon. Thin oxide layers form under reactive conditions when metals are exposed to oxidizing conditions; the formation of passive films guarantees corrosion protection of metals.[125,126] Today two-dimensional oxides are studied as ultrathin capacitors,[127] for solar energy materials,[128] for magnetoresistance sensors,[129] etc.[130]

In the last two decades, oxide ultrathin films have become interesting also in heterogeneous catalysis. They have been prepared as model systems to develop concepts of electronic/geometric structure–reactivity relations to be transferred to the properties of real catalysts. Those ultrathin films allow the application of electron spectroscopies and scanning probe microscopies (SPM) to aim at their characterization at the atomic level.[131–135] Specific techniques have been developed to grow epitaxial oxide films, deposit metal nanoclusters, and study their chemistry under controlled conditions. In general, while ultrathin oxide films may closely resemble the corresponding bulk counterparts, other ultrathin film oxides exhibit completely different properties. Particularly interesting in this context is the possibility of selectively charging atomic or molecular species adsorbed on an oxide ultrathin film.[136,137] Electrons may tunnel through the insulating thin layer, leading to charged surface species supported on oxide thin films. The charge transfer then results in completely different chemistry and catalytic activity.

A number of studies have indicated that non-reducible oxides may be especially suitable for thin film growth[116,138–143] when a well-adapted metal support to allow for epitaxial growth was used. MgO, CaO, Al_2O_3 and SiO_2 are examples. Typically, ultrahigh vacuum conditions and physical vapor deposition in an oxygen atmosphere are used so that the material is free of any contaminant,[140] which for reliable experimental studies is a non-debatable prerequisite. Fig. 9 shows for MgO(100) grown on Ag(100) that those films exhibit the geometric characteristics of their bulk counterparts and even the physical and chemical properties are very similar if those films are grown to a certain thickness. Electron diffraction (low energy electron diffraction, LEED) and electron spectroscopies (electron energy loss spectroscopy, EELS, and ultraviolet photoelectron spectroscopy, UPS) for films of various thicknesses indicate that the properties, such as geometric structure, phononic properties and even the band gap of 6 eV (differential conductance measurements using STM), for films of a few monolayers correspond closely to those of a MgO(100) single crystal.[141,142,144–148] Density functional calculations support the experimental results.[149] The defect free MgO surface[150,151] is quite inert, at variance with a defect rich surface (see Section 2.2), and the defect density may be controlled by the preparation conditions, induced by the STM tips by operation at high voltages and high currents, or by the choice of the metal substrate.[152] Mo(100), for example, exhibits a larger misfit to MgO, which favors the formation of defects, in particular steps and kinks as well as point defects, such as color centers (oxygen vacancies).
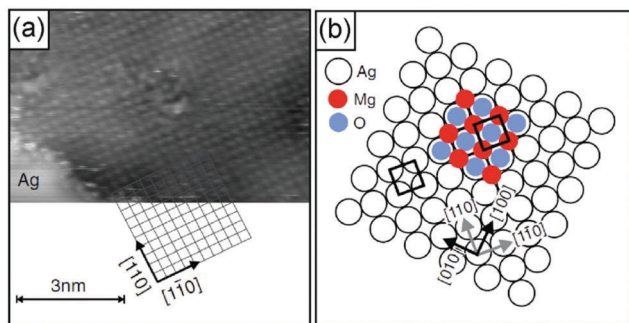
This journal is © The Royal Society of Chemistry 2018

Chem. Soc. Rev., 2018, **47**, 8474–8502 | 8485

Fig. 9 (a) Atomic resolution indicating the lattice orientation of the substrate (I_t = 2 pA, V_t = 30 mV). Subsequently, atomic resolution of an MgO film surface has been achieved by site specific dynamic force microscopy (AFM).[157] (b) Growth model of MgO/Ag(001). Illustration of the most favorable configuration: Mg-atoms occupy hollow sites, i.e., they continue the Ag fcc lattice (lattice constant a = 0.409 nm), and O-atoms occupy on top sites. The Ag(001) surface unit cell is indicated. From ref. 149 and 158.

Fig. 10 Low energy electron diffraction diagrams and STM topographic images of the respective systems, i.e. (a) and (d) a silica monolayer on Ru(0001), $SiO_{2.5}$/Ru(0001), (b) and (e) a crystalline bilayer and (c) and (f) a vitreous (amorphous) bilayer, SiO_2/Ru(0001).[163,166] Adapted with permission from ref. 166. Copyright American Chemical Society, 2012.

Those point defects are traps for electrons, which may be transferred to adsorbates (metal atoms or molecules, see Section 2.2.1).[153–155] The point defects (color centers) come in different flavors, depending on how many electrons have been trapped. They are called F^0, F^+ or F^{2+} centers for two, one and no electrons trapped. A combination of scanning tunneling spectroscopy and high-resolution Kelvin probe force microscopy allows the identification of the various color centers.[104,156] It is found that most of them but not all are localized at kinks and steps, since the energetic cost for its formation is considerably lower than that on terraces.

As stated above, the films are prepared by physical vapor deposition onto a metal substrate, followed by an annealing step to order the surface structure. Depending on the annealing temperature, diffusion of metal atoms (dopants) from the substrate into the oxide film has been observed. This has been studied in detail for CaO(100) films grown on top of a Mo(100) surface. The state of the dopant may be probed using XPS, whereby the depth distribution of the dopants may be analyzed using angle dependent XPS or photon energy dependent spectra via synchrotron radiation studies via an effective variation of the electron escape depth.[120,159–161] Another way to bring the dopant into the film is successive evaporation of a film of a given thickness, followed by the evaporation of the dopant material and a second controlled film deposition step to bury the dopant. This allows for a controlled deposition of the dopant at a given depth below the oxide surface.

Another example for an oxide film with great potential in model catalyst preparation is SiO_2.[162,163] Ultra-thin silica films have been grown using similar recipes to those for MgO on a number of metal single crystal surfaces. Depending on the oxygen affinity of the metal substrate, either single layers directly bound to the metal substrate or bi-layer films, only van der Waals bound to the substrate, or both on the same substrate, have been prepared.[164,165] In particular, bilayer films were thoroughly studied with respect to their structure with a particular emphasis on the analysis of crystalline and amorphous structures.
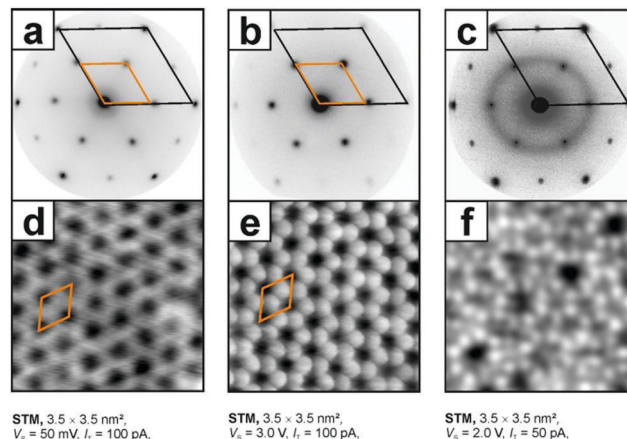
Ru(0001) is the metal substrate on which both monolayer and bilayer films have been prepared. They have been experimentally studied and characterized using STM, LEED, infrared reflection absorption spectroscopy (IRAS) and XPS. Fig. 10 shows electron diffraction patterns and scanning tunneling images of the films together with structural models, which have been established on the basis of the experimental data in combination with density functional calculations.

The structural principle is based on corner-connected SiO_4-tetrahedra forming a two-dimensional structure of six-membered rings. In the mono-layer films one corner of the SiO_4-tehedra is directly bound to the metal substrate, while in the bi-layer films a second, flipped layer of corner-connected SiO_4-tetrahedra is bound from below directly to the top layer forming Si–O–Si bonds between the layers. In contrast to the monolayer, the bi-layer exhibits perfect SiO_2 stoichiometry. Since all the constituting atoms are valence saturated, the bi-layer film is only bound to the metal by dispersion forces. This bi-layer film exists both in a crystalline and in an amorphous phase as is convincingly demonstrated using scanning tunneling images. It represents the first example of an amorphous oxide film, where the structure is identified down to the atomic level.[167] It proves the model for amorphous silica proposed by Zachariasen in 1932.[168] He proposed a model where the SiO_4-tetrahedra are still corner connected but form rings of different sizes ranging from 4-membered to 9-membered rings. Detailed investigations prove that the bi-layer film corresponds perfectly to the Zachariasen model, and may also be used in comparison to 3-dimensional silica. With respect to the present review it is important to mention that the amorphous bi-layer represents a model for an amorphous silica support, a material often used to fabricate real catalytic materials. Examples are heterogenized homogeneous catalysts, where metal complexes are bound to an amorphous silica substrate. An industrially important example is the Phillips catalyst for ethylene polymerization.[169–172] In this system, chromium

8486 | Chem. Soc. Rev., 2018, **47**, 8474–8502

This journal is © The Royal Society of Chemistry 2018

atoms are bound to the silica, and the exact bonding situation is claimed to be relevant to understand the detailed mechanism of the polymerization reaction.[173–181]

This brings us to another aspect: in order to bind metal atoms, in particular to amorphous silica, the film has to be hydroxylated. This turns out to demand a special methodology due to the stability of the film. Only *via* electron bombardment in the presence of water does hydroxylation turn out to be possible.[182,183] For details we refer to the original literature. However, oxide film hydroxylation, in general, is an important aspect also, and in particular with respect to MgO.[184] In the latter case, hydroxylation is important depending on the chemical nature of the metal bound to the oxide surface. If one attempts to understand the basic mechanisms of wet impregnation techniques, it is obviously crucial to investigate the bonding not only to pure oxide surfaces, but also to those hydroxylated. In general, one needs to realize that understanding chemical modification of oxide surfaces is prerequisite to be able to mimic the complexity of real catalyst systems.[185]

Once the oxide films have been prepared, the final step in the preparation of a metal–oxide supported model catalyst system is the deposition of the metal particle.[116] Basically two different approaches have been used. One, the simpler technique, is the diffusion-controlled growth of particles after physical vapor deposition of a given metal.[116,139,140,186] The other, more technically demanding one, is deposition of size-selected clusters prepared by laser vaporization of the chosen metal in a He-atmosphere or by He-ion sputtering and subsequent mass-selection in a quadrupole mass filter.[140,187,188] In the following sub-section we will discuss a number of examples of metal nano-particles on ultrathin oxide films, also with respect to charge control.

3.2 Nano-particles on ultrathin oxide films

Individual Pd atoms on an ultrathin alumina were imaged first by Nilius *et al.* in 2003,[189] after theoretical predictions had been published for alumina and MgO. Those theory papers predicted a positive charge for the Pd on alumina and a neutral Pd atom for MgO.[190,191] Experimentally, evidence for the charge state of the metal atom could not be provided. Clear experimental indications on the charge state of individual metal atoms on thin films were provided using STM studies on Au atoms deposited on a NaCl films grown on Cu single crystals by applying voltage pulses to the tip, and thus changing the charge state of the atom.[192,193] On oxide films clear evidence was provided *via* STM and theory[194,195] for negatively Au atoms and neutral Pd atoms on MgO(100) in comparison with density functional calculations. The Pd atoms reside on the O ions, while negatively charged Au atoms reside on Mg or on hollow sites.[194,195] Fig. 11 shows a comparison of the distribution of Au atoms in Fig. 11a and Pd atoms in Fig. 11b. Due to the negative charge the Au atoms carry, and the associated Coulomb repulsion to other negatively charged species, the Au atoms repel each other, which leads to the observed non-statistical spatial distribution, while the neutral Pd atoms clearly exhibit a statistical distribution.
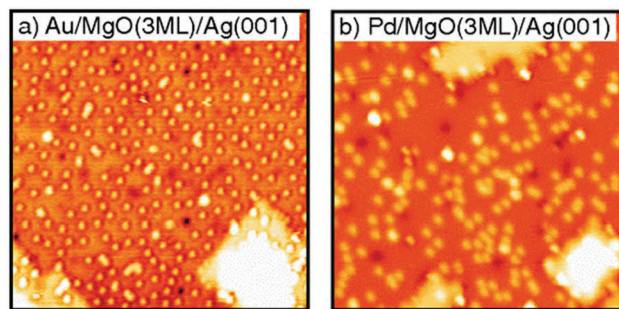

Fig. 11 STM images (30 × 30 nm²) of (a) Au atoms (θ = 2.9% ML Au) adsorbed on 3 ML thin MgO films (V_s = 0.5 V, I_t = 11 pA); and (b) Pd atoms (θ = 2.3% ML Pd) adsorbed on 3 ML thin MgO films (V_s = 0.2 V, I_t = 13 pA). Reprinted with permission from ref. 195. Copyright 2007 by the American Physical Society.

A series of studies on metal atom aggregates have been reported. The first study to experimentally determine charge transfer by STM conductance imaging of metal aggregates was reported in 2008 in combination with a computational effort by the Sauer group.[37] As shown in Fig. 12 the conductance images of linear Au chains on alumina/NiAl(110) with varying lengths represent the quantum states of the systems created by the Au 6s electrons.

Identifying the states below and above the Fermi energy and knowing the number of atoms involved in the Au chain allow
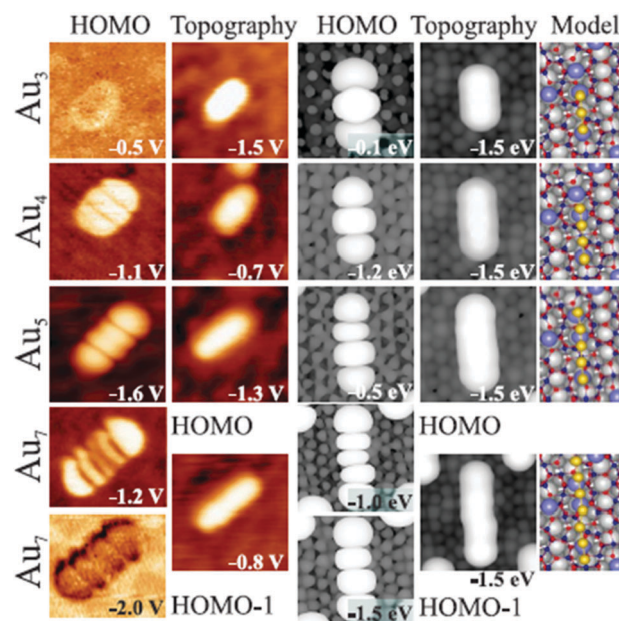

Fig. 12 Experimental conductance images of the Au chain states representing the ground state and calculated HOMO (highest occupied molecular orbital) shapes, topographies, and model structures for Au₃, Au₄, Au₅, and Au₇ chains. Images are 5.0 × 5.0 nm² in size. For the Au₇ chain, a second state at higher imaging voltage in addition to the HOMO−1 are shown. Measured chain lengths are 0.9 nm, 1.2 nm, 1.5 nm, and 2.2 nm; calculated distances between the first and last chain atoms amount to 0.53, 0.78, 1.05, and 1.55 nm. To compare theoretical to experimental lengths, 0.2 to 0.3 nm should be added to both chain sides to account for the diffusivity of the 1D orbitals. Reprinted with permission from ref. 37. Copyright 2008 by the American Physical Society.
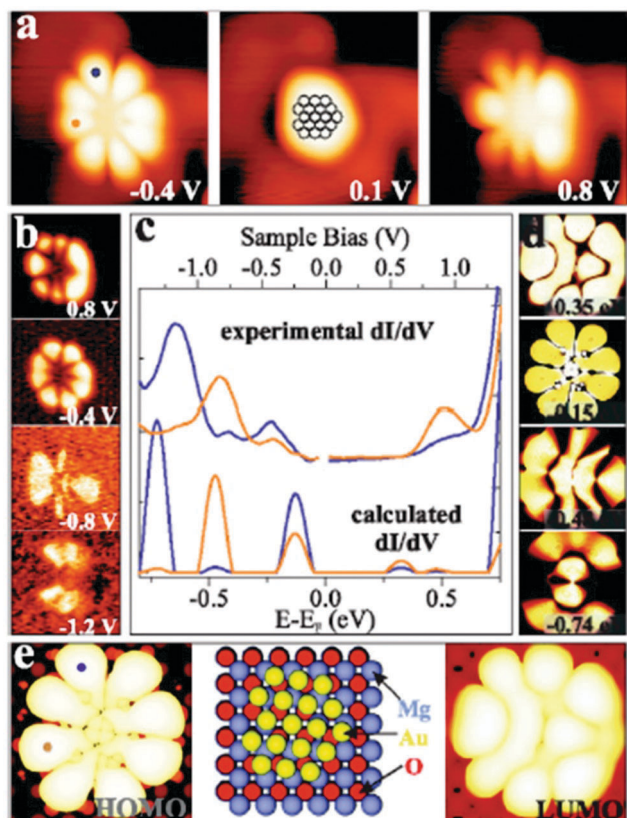
Fig. 13 (a) STM topographic and (b) conductance images of a Au_{18} cluster on 2 ML MgO/Ag(001) (I_t = 5 pA, 3.9 × 3.9 nm^2) in comparison with simulated (d) conductance and (e) topographic images (2.0 × 2.0 nm^2) and a structure model. (c) Experimental and simulated dI/dV spectra recorded at the blue and orange dots marked on the cluster in (a) and (e). Reprinted with permission from ref. 38. Copyright 2009 by the American Physical Society.
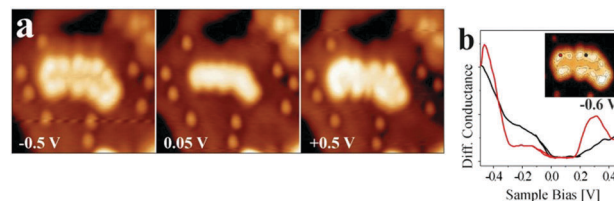

Fig. 14 (a) Conductance spectra recorded on a kink and a step position of the island shown in the inset. The bias set point was +0.5 V. The locally increased density of states at the cluster rim is clearly observed in (a) and (b), indicating the presence of a negatively charged 2D-Au cluster. Reprinted with permission from ref. 39. Copyright 2010 by the American Physical Society.

counting the number of electrons in the chain. The idea is to use the concept of a particle-in-a-box and to count the nodes in the electron densities of states as a function of energy. This leads in the case of the Au_7 chain to the result that three electrons must have been transferred in addition to the electrons provided by the Au atoms in the chain. An important prerequisite is, of course, that the number of atoms is known, which restricts a detailed analysis to relatively small aggregates. Another example for a somewhat larger two-dimensional aggregate is shown in Fig. 13.[38]

This figure is based on an experimental study by Lin et al.,[38] in collaboration with the Häkkinen group, providing the theoretical input. A Au_{18} cluster has been identified, and by applying the same procedure as outlined above for the linear chain, but adapted here to the two-dimensionality of the object it is concluded that 4 extra electrons have been transferred to the flat Au particle. In an attempt to generalize this procedure to larger objects of 100 atoms or more and arbitrary shapes it is found, as alluded to above, that a strict purely experimentally based analysis is difficult. However, based on calculations in comparison to experiments on larger islands it was noticed that the extra charge tends to be localized at the rim of the object.[39] This is documented in Fig. 14 where STM topographic images of two-dimensional larger Au islands are shown.

Fig. 14b presents the filled and empty states of a Au island and illustrates the localization at the rim of the nano-particle. We note here that the electron localization at the rim occurs through electron transfer from the metal substrate, while the mixing of the electronic states of the metal underneath the film and the metal nano-particle on top of the film is negligible. Are there conventional ways by XPS to verify the negative charge on the particles? To answer this question, an Auger parameter study was carried out for flat Au particles.[181] Wagner established the Auger parameter concept and showed that the changes in the difference between the binding energies (BEs) of XPS and kinetic energies (KEs) of Auger peaks from a given atom are related to changes in the final state, i.e. the ion state, of the atom exclusively via the following equation:[196]

$$\Delta\alpha = \Delta(BE_{XPS} + KE_{Auger}) = 2\Delta R, \tag{2}$$

where R is defined as the relaxation contribution to the final state of any levels of BE. This, however, was shown to be empirically false[197,198] when comparing changes in valence and deeper core levels. To circumvent this problem, a modified Auger parameter was created:[199]

$$\Delta\beta = \Delta[2E_B(i) - E_B(j) + E_{Kin}(jii)] = 2\Delta R_i. \tag{3}$$

where (i) and (j) refer to the leads of the atom involved.

This definition does no longer require the assumption of equal relaxation for all levels. Details are described in the literature.[181,199,200] Since the relaxation energy may be calculated from this relation in a straightforward manner and the difference in binding energy is the difference between the initial state shifts, i.e. the difference in the Koopmans energies of the involved level, the initial state shift may be extracted. This shift is directly correlated with the charge the core level experiences. Fig. 15 compiles the data for the Au nano-particles on MgO(100)/Ag(100) as a function temperature.

The temperature has been varied because it has been learned that at a temperature higher than 550 K the particles start to lose their flat morphology. Clearly, the initial state shifts of the Au particles are strong and negative, consistent with the negative charge on the Au particles. However, the final state shifts are even bigger and overcompensate for the initial state shifts, thus leading to an observed chemical shift, which, would it be taken to represent the charge state, would have led
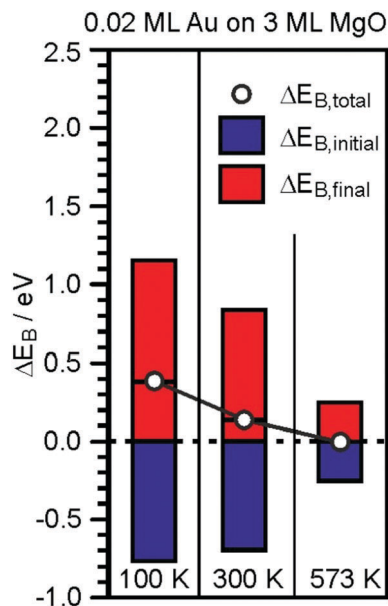
Fig. 15 Graphical representation of the EB-shifts derived from XPS and Auger measurements for 0.2 ML Au on 30 ML MgO(001)/Ag(001) with reference to Au(111).[181]

Fig. 16 (a) STM topographic images of (a) a pristine planar Au cluster and (b) after exposure to CO_2 (scan size 8.0 × 8.0 nm^2, 50 pA). The Au clusters were prepared by evaporating Au on MgO mono- or bilayer films at 300 K. Subsequently, the sample was exposed to 10–15 L CO_2 in a temperature range from 220 to 250 K. Molecules at the cluster perimeter in (b) become visible only when scanning at bias voltages between −0.5 and +0.5 V. (c) Corresponding dI/dV map, displaying the high localization of electron density at the negatively charged cluster rim. (d) dI/dV spectra recorded at the center of the clusters shown in (a) (blue) and (b) (red). The positions of the first (I) and third (III) quantum well states in both spectra are indicated. Note the energy shift towards higher energy of the internal energy scale of the cluster which is compatible with a CO_2 induced decrease of the electron potential well formed by the Au island. Reprinted with permission from ref. 202. Copyright 2015 Wiley-VCH.

to wrong conclusions. In comparison to the Au particles on the ultrathin MgO film, a similar study has been performed for a similar amount of Au deposited on a thick (60 layers) MgO film, representing bulk MgO.[181,201] The particles exhibit a three-dimensional morphology, which was predicted by computations to not exhibit strong charge transfer to the Au particles,[118] and thus no reactivity towards CO_2 (see below). The negative initial state shifts are missing and the results are consistent, indicating that the presented approach to determine charge transfer is valid and corroborates theory.

Very recently, Calaza et al.[202] were able to correlate the electron localization at the rim of Au nanoparticles with chemical reactivity. Carbon dioxide was used as a probe. A set of STM topographic images (a–c) of the reactive system together with differential conductance curves as a function of bias voltage (d) are shown in Fig. 16.

The visible protrusions have been identified as oxalate anions $(C_2O_4^{2-})$ via infrared spectroscopy. This may sound surprising! However, while CO_2 is a thermodynamically very stable molecule requiring 0.6 eV to transfer an electron to form a CO_2-anion, a CO_2-dimer, for example, forms an anion exothermically with a gain in energy of approximately 0.9 eV.[202–204] The barrier for formation is, of course, the energy to bend the linear molecule. This observation is fully in line with the observed reactivity of CO_2 on alkali (i.e. electron enriched) metal surfaces.[205] Clearly, the reactivity is linked to the electron localization at the rim of the nano-particle. The fact that this may be directly observed using scanning probe techniques is a consequence of the flat morphology of the nano-particle. Had the particles been three-dimensional with a regular aspect ratio observed in real catalysts, this would not have possible, as attempts to directly image reactivity at the rim have failed so far.[40] The present system allows for an even more in depth
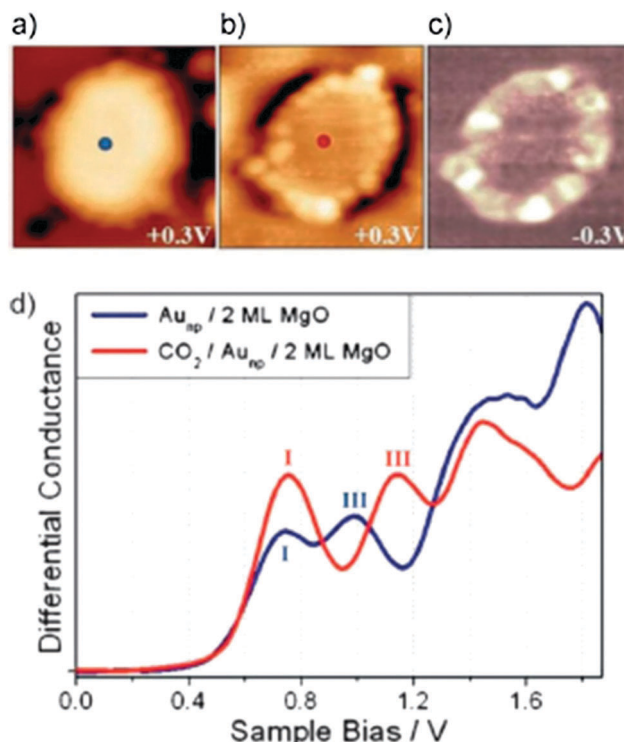
analysis of the electronic structure. As indicated in Fig. 16d, the quantum well states of the Au nano-particles shift as the molecules cover the nano-particle rim. A detailed analysis[206,207] shows that the observed shifts are compatible with a situation where the electrons occupying Au quantum well states are energetically shifted to higher values because of the presence of the extra negative charge on the molecules at the rim. This observation reveals how molecular adsorption modifies the properties of metal nano-particles, a topic of importance in heterogeneous catalysis.

At this point, a word about inverse catalysts appears to be in order.[208,209] When one deals with reactivity at oxide–metal interfaces, so far we have chosen the approach to place the metal nano-particle on top of an oxide film in order to mimic the situation encountered in real catalysts. Another option chosen by some researchers is to create an oxide film on top of a metal surface (representing the metal the nano-particle is made of) and not fully cover the metal surface, so as to leave the oxide–metal interface open and accessible.[210–212] A schematic is shown in Fig. 17.
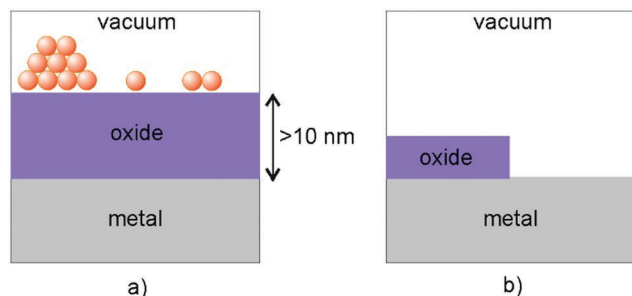
Fig. 17 Schematic illustration of (a) a "regular" model system and (b) one representing an "inverse" catalyst. Adapted with permission from ref. 208. Copyright 2016 American Chemical Society.

Some researchers call this an inverse catalyst (inverse with respect to metal-particles on oxides) and claim that this allows interrogation of the interface in the same way as for the metal particle on top of the oxide support. This nomenclature is somewhat misleading, as it implies that for the interface it does not matter whether one investigates metals on oxides or oxides on metals. Obviously, this is incorrect, because the details at the interface will be rather different. Still those investigations are useful in their own right, as they are encountered in specific situations in catalysis, in particular, in so-called SMSI situations described in the Introduction,[26,213–220] as we will see in the final chapter.[208]

Having raised this issue of whether the support–metal interface is properly represented, some more considerations are appropriate. One specific comment concerns here the investigation of compound nano-particles on metal substrates, where the metal only represents a platform to investigate the compound particle *per se*. We discuss here an example put forward by the Besenbacher group investigating MoS_2 nano-particles on Au substrates.[221] As shown in Fig. 18 they were able to present beautiful atomically resolved STM images revealing the triangular morphology of the particle.

The geometric parameters deduced from the STM images are fully consistent with the geometric parameters of the basal plane of bulk MoS_2. However, the hexagonal basal plane would have suggested hexagonal nano-particles, while triangular particles are observed. This implies that the different edge terminations exhibit different stabilities. In comparison with calculations it was found that the observed edge structure is only obtained when the stoichiometry on the edges changes, in the sense that only one S atom is bound to the Mo edge atom. This is, of course, important to understand those MoS_2 nano-particles. However, the influence of the Au template (substrate) needs to be considered as well. In the spirit of the inverse catalyst approach, we must ask the question whether the extended Au substrate does not influence the morphology of the sulfide-nano-particle *via* direct coupling of the electronic structure of the Au with the sulfur of the MoS_2. Given the strong affinity of sulfur to Au, this is not unlikely.

3.3 Polaronic distortion: a response to the formation of charged adsorbates

The study of charge transfer phenomena occurring on oxide ultrathin films has shown that the effect is accompanied by
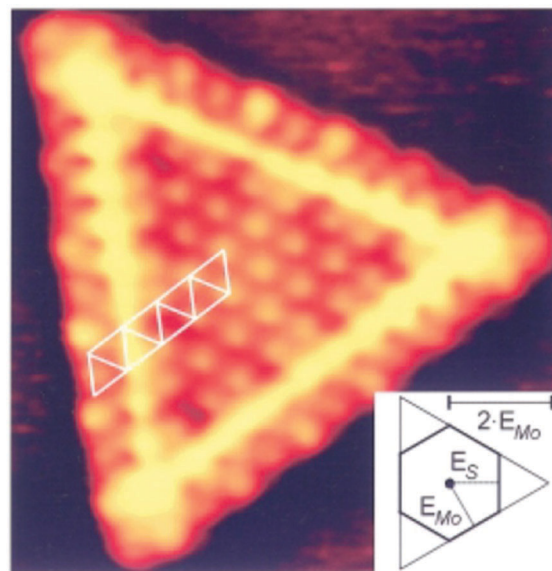

Fig. 18 An atom-resolved STM image (scan size 4.1 × 4.1 nm², I_t = 1.28 nA, V_t = 5.2 mV) of a triangularly shaped single-layer MoS_2 nanocluster. The grid shows the registry of the edge atoms relative to those in the basal plane of the MoS_2 triangle. The inset shows a Wulff construction of the MoS_2 crystal. E_{Mo} and E_S denote the free energies for the Mo and S edges, respectively (from ref. 221). The lines of highly increased contrast following the edges of the MoS_2 triangles were shown to originate from one-dimensional metallic edge states in MoS_2. Reprinted with permission from ref. 222. Copyright 2001 by the American Physical Society.

non-negligible structural relaxation. The geometrical response to the charge transfer turns out to be essential for the stabilization of the charged species and, in general, for the properties of the films. Ultrathin films possess a structural flexibility, which has no correspondence on bulk surfaces. In this section we will provide some examples to discuss the effect and demonstrate its role in charge transfer properties and even catalytic reactions.

As we mentioned above, gold atoms exhibit completely different adsorption properties when deposited on bulk MgO or on an ultrathin MgO film supported on a metal: while they remain neutral on MgO(100), they become negatively charged on MgO/Mo(100) or MgO/Ag(100) ultrathin films.[194,195] The net charge transfer takes place *via* spontaneous electron tunneling, provided that the film thickness remains below the mean-free paths of electrons. This effect is always accompanied by a structural relaxation of the films.

As an example we consider a Ag atom adsorbed on MgO/Mo(100) films.[223] Here Ag becomes a full anion according to DFT calculations, which also show a non-negligible local relaxation in the MgO top layer. This can be quantified by the change in vertical distance, Δz, of a given ion of the surface before and after adsorption of the Ag atom, Table 1. If the Ag atom is adsorbed on a bare MgO(100) surface (here represented by 3 ML MgO films), the displacements of the O or Mg ions to which Ag is bound, Δz, and of the first neighbors are very small (<0.02 Å in absolute values). If the Ag is now adsorbed on MgO(3 ML)/Ag(100) films the displacements become substantial, Δz = 0.1–0.2 Å, Table 1: in

Table 1 Local surface relaxation on MgO 3L slabs induced by adsorption of a Ag or Au atom

		On top of O		On top of Mg	
		Δz_O (Å)	Δz_{Mg} (Å)	Δz_O (Å)	Δz_{Mg} (Å)
Ag_1 on	MgO(100)	+0.01	+0.02	−0.02	−0.01
Ag_1 on	MgO/Mo(100)	−0.08	+0.09	−0.03	+0.23
Au_1 on	MgO(100)	−0.04	+0.03	−0.02	+0.01
Au_1 on	MgO/Mo(100)	−0.20	+0.15	−0.03	+0.36

Table 2 Measured and computed g-tensors for O_2^- adsorbed on the surfaces of MgO/Mo(001) films and MgO powders

	Method	Site	g_{xx}	g_{yy}	g_{zz}	Δg_{zz}
MgO powders	Exp.	Terrace	2.002	2.008	2.091	0.000
MgO powders	Exp.	Edge	2.002	2.008	2.077	−0.014
MgO/Mo(100)	Exp.	Terrace	2.002	2.012	2.072	−0.019
MgO(100)	Theory	Terrace	2.0022	2.0092	2.0639	0.0000
MgO(100)	Theory	Edge	2.0021	2.0096	2.0527	−0.0112
MgO/Mo(100)	Theory	Terrace	2.0025	2.0093	2.0560	−0.0089

particular, when Ag is adsorbed on top of an O^{2-} ion the downward displacement is 0.08 Å; the neighboring Mg cations move up by about the same amount. If, however, the negatively charged Ag atom is positioned on top of a Mg cation, the displacement of this ion from the MgO top layer is rather large, 0.23 Å, Table 1.

The effect is even more pronounced for Au. This is shown by the Au–MgO distances: on MgO/Mo(100) films the Au–O^{2-} distance (2.76 Å) is 0.52 Å longer than that on the bare MgO(100) surface, and the Au–Mg distance (2.57 Å) is 0.13 Å shorter. Thus, the formation of a Au anion is accompanied by a large surface relaxation, at variance with Au on MgO(100). On MgO/Mo(100) 3 ML films, Au atom adsorption on Mg is accompanied by an outward displacement of the cation by 0.36 Å; Au adsorption on O induces a downward displacement of −0.20 Å (and an outward movement of the neighboring Mg cations by 0.15 Å, Table 1).

These geometrical relaxations are typical of the formation of a small polaron in an insulating material and provide an important contribution to the stabilization of the adsorbed species. To prove this, a computational experiment has been designed where the MgO ultrathin film is not allowed to relax in response to the adsorption of a Au (or Ag) atom. Interestingly, if no relaxation is allowed, the charge transfer is suppressed and the formation of the Au^- species is not observed. Hence, the charge transfer is a direct consequence of the structural deformation of the two-dimensional oxide in response to charge localization on the Au adsorbate.

The formation of negatively charged adsorbates is not restricted to Au. Molecular oxygen can induce an electron transfer and form superoxo species. The formation of O_2^- species on MgO/Mo(100) films exposed to oxygen has been predicted theoretically[224] and confirmed by low temperature EPR spectra.[225] The EPR study shows that for films containing 15 ML of MgO, the EPR signal disappears, indicating the suppression of the electron transfer if the oxide film becomes too thick and in full agreement with the model of charge transfer *via* electron tunneling. Particularly interesting for the present discussion is the analysis of the g-tensor of the O_2^- species formed on MgO/Mo(100) films, Table 2. This, in fact, provides experimental evidence that indeed the MgO film undergoes a polaronic distortion in response to the formation of the O_2^- species.

The EPR experiments, performed under ultrahigh vacuum conditions at 40 K on a 4 ML thick MgO/Mo(100) film, give the following components of the g-tensor: g_{xx} = 2.002, g_{yy} = 2.012, and g_{zz} = 2.072. Similar measurements exist for O_2^- species

formed on the surfaces of MgO polycrystalline materials,[226–228] where the superoxo species forms by interaction of O_2 with electron-rich, defective sites at the surface of the material. Thus, it is possible to compare the values of the g-tensor found on the thin MgO/Mo(100) films with those obtained on the surfaces of MgO powders. The x- and y-components of the tensor are not too different, while a significantly larger z-component is found on powders compared to thin films: g_{zz} = 2.091 on the (100) terrace sites of MgO powders, and g_{zz} = 2.072 on the terrace sites of MgO/Mo(100), Table 2.

These differences, small but significant, can be explained with the help of theory. The g-tensor has been computed for an O_2^- radical adsorbed on a MgO cluster modeling the MgO(100) surface, Table 2. With respect to the measurement on the MgO powder samples, the g_{xx} and g_{yy} components are well reproduced, while the g_{zz} component is slightly underestimated in the calculation (the g_{zz} component is systematically underestimated in calculations). However, what is relevant is the trend found comparing the computed g-tensors of O_2^- on terrace, Mg_{5c}, and edge, Mg_{4c}, sites. There is a reduction of the g_{zz} component, Δg_{zz}, by lowering the coordination number of the Mg ion, Table 2. Now we come to the implications of this result for the discussion of the polaronic distortion in thin films. The value of the g_{zz} tensor measured for the MgO/Mo(100) thin films is closer to that measured on MgO powders and assigned to Mg ions at low-coordinated edge sites. But it can be demonstrated that on the thin MgO/Mo(100) films O_2^- forms on the flat terrace sites, not on the edges. So why are the g_{zz} values similar in the two cases? The answer is the polaronic distortion. A calculation which includes the polaronic distortion of the MgO/Mo(100) thin film shows in fact a considerably reduced g_{zz} component, as observed experimentally, Table 2.[225]

To better understand this effect, it should be reminded that the shift of the g_{zz} component from the free electron value is given by $g_{zz} = g_e + 2[\lambda^2/(\lambda^2 + \Delta^2)]^{1/2}$, where λ is the spin–orbit coupling constant and $\Delta = 2\pi_g^y - 2\pi_g^x$ is the strength of the local electric field. A more exposed cation, as on the edge sites of the MgO powders, or on the terrace sites of the MgO/Mo(100) thin films when the polaronic distortion is present, leads to a reduction of g_{zz}. This is exactly what is found both in theory and in experiment. The smaller value of g_{zz} for O_2^- on the MgO thin film is thus direct proof of the occurrence of a polaronic distortion.

Another confirmation of the structural flexibility of oxide ultrathin films comes from the study of XPS line broadening.[229] XPS is usually based on the analysis of the areas and positions

This journal is © The Royal Society of Chemistry 2018
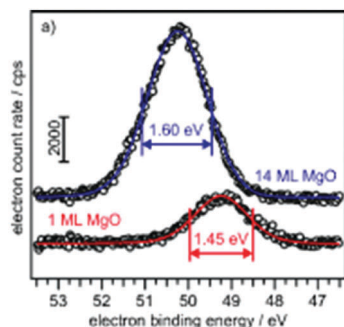
Chem. Soc. Rev., 2018, 47, 8474–8502 | 8491

Fig. 19 Experimental Mg 2p XPS spectra of 14 ML and 1 ML MgO/Ag(100). Adapted from ref. 229. Copyright 2011 Wiley-VCH.

of photoemission peaks. Vibrational excitations lead to broadening in XPS, connected to the change in the nuclear geometry at equilibrium between the initial ground state and the final excited or ionized state. Since the flexibility of thin oxide layers is connected to the phonon structure of the material, one can look at the broadening in photoelectron spectra to investigate the vibrational properties. In particular, changes in the initial-state polaronic distortion can affect the final-state changes in bond length. Comparing the line widths of MgO ionizations in single crystals or thick MgO films and an ultrathin MgO/Ag(100) film (Fig. 19), it has been possible to obtain a direct indication of the changes in structural flexibility.

Fig. 19 shows the experimental Mg 2p XPS spectra of 1 and 14 ML MgO/Ag(100) films. For 1 ML MgO/Ag(100) the full width at half maximum (FWHM) of the Mg 2p peak is 1.45 eV; this becomes approximately 1.60 eV for 10 ML and thicker MgO films. The reduction in the broadening for the thin layer is predicted by theory based on pure Frank–Condon broadening. The Frank–Condon broadening for 1 ML MgO differs from those of thick MgO films (bulk-like) because the equilibrium Mg–O distance, r_e, is different for bulk and monolayer MgO; this is true for both the ground state and the 2p hole potential curves. Also the curvatures of these potential curves, as measured by ω_e, are different between bulk and monolayer MgO, and provide a measure of the softness of the phonon modes of the 2D oxide.

The softness of the ultrathin films is not restricted to MgO. Going to SiO_2, for instance, other pieces of evidence of the softness of the thin films come from the study of their adsorption properties. Crystalline SiO_2/Mo(112) monolayer films have been investigated in detail by experiment and theory.[230–232] The structure of these films has been described in Section 3.1. The film consists of hexagonal rings interrupted by eight-membered rings along line defects. Spontaneous charging of deposited gold does not occur on pristine SiO_2/Mo(112) films: both experiments and calculations show that gold atoms interact very weakly with the surface, diffuse and aggregate to form Au nanoparticles in correspondence to the line defects.[233,234] However, a possible way to modify the film reactivity is to dope the system with alkali metal atoms which form M^+ ions stabilized above the silica film or at the SiO_2–Mo(112) interface, depending on the size. For instance, Li atoms diffuse

spontaneously through the six-member rings of the silica film to the interface where they form stable Li^+ ions. The interface Li ions cannot interact directly with the deposited Au atoms which are adsorbed on the silica surface. The presence of Li^+ ions lowers substantially the work function Φ (up to 1 eV for a full coverage $\theta = 1$ corresponding to one interface Li atom per silica ring). Au atoms deposited on the Li-doped SiO_2/Mo(112) film show properties that differ completely from those of the corresponding undoped system.[235,236] On some surface sites the Au atom becomes strongly bound, by 1.33 eV, and negatively charged $(-0.80\ e)$. With the help of STM images it has been possible to verify that the Au atoms are effectively stabilized above these specific sites of the film. Notice that the charge transfer, and hence the stabilization of Au^-, is possible only on these specific adsorption sites:[237] this is connected to the strong polaronic distortion which stabilizes the charged state of the Au^- anion. DFT calculations show that on these sites the O atom of the top layer relaxes towards the Mo surface by about 0.85 Å, while the two adjacent Si atoms move towards the Au anion by about 0.1 Å. This relaxation strongly stabilizes the 6s level of Au, which becomes doubly occupied with the formation of Au^-. As for MgO/Ag(100), if the polaronic distortion is not allowed, then the charge transfer does not take place.

3.4 Electrostatic origin of rumpling in supported oxide thin films

Structural relaxation in supported oxide films can be substantial also without the presence of adsorbed species. In this case the relaxation is not local and it involves the entire film. It can be measured by the extent of rumpling, defined as the separation between the atomic planes of cations and anions of a monolayer. In general, the rumpling for unsupported monolayers is negligible;[238] however, this can become substantial if the oxide film is deposited on a metal, and depends on the electronic properties of the metal substrate.[239] The occurrence of charge transfer at the metal/oxide interface generates an electric field which, in turn, causes the rumpling of the oxide film. If the oxide film is deposited on a metal with high electronegativity (high work function), charge is transferred from the oxide to the support; in this case the anions in the oxide layer are pushed outwards, Fig. 20a, for electrostatic reasons.[240] Of course, the opposite is also true. A substrate with low electronegativity (small work function) favors electron flow towards the oxide, and in this case it is the oxide cations that are displaced outwards, Fig. 20b. In this respect, the rumpling in the thin supported film is simply the structural response to the charge transfer occurring at the metal/oxide interface.

The rumpling in the oxide layer generates a dipole (D_R) with the opposite sign with respect to that due to charge transfer at the interface (D_{CT}). The two effects go in opposite directions. This is well demonstrated by DFT calculations showing that MgO monolayers interfaced with electropositive metals (Al and Mg) induce electron transfer from the metal to the oxide and a negative rumpling (oxygen closer to the metal surface, Fig. 20b); MgO monolayers deposited on metals with large work functions (Ag, Mo and Pt) induce electron transfer from the oxide to
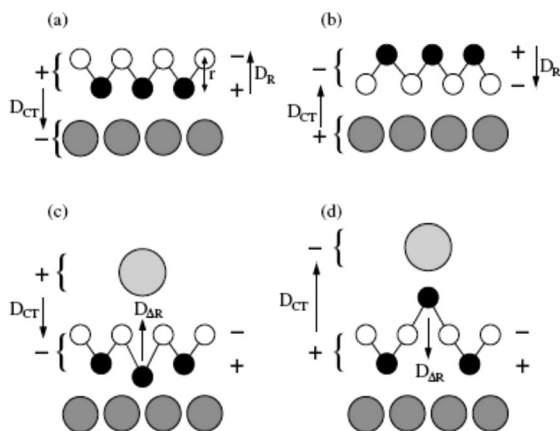
Fig. 20 (a and b) Schematic representations of the coupling between dipole moments due to charge transfer at the interface (D_{CT}) and due to rumpling (D_R) in oxide monolayers (black circles = cations, white circles = anions) deposited on a metal substrate (large gray circles). (c and d) Schematic representations of ''direct'' (c) and ''flipped'' (d) adsorption modes of an adatom (large circle) on a supported oxide film. Direct adsorption mode: the polaronic-like distortion induced by the adatom increases the rumpling (distance between planes of anions and cations); flipped adsorption mode: the distortion reduces the rumpling. Dipole moments due to the charging of the adatom (D_{CT}) and to the adsorption-induced structural distortion (D_R) are plotted schematically with arrows. Adapted with permission from ref. 240. Copyright 2009 by the American Physical Society.

the metal, and a positive rumpling (oxygen relaxes outwards), Fig. 20a.

In a similar way, the adsorption of an atom, a molecule or a small cluster, when accompanied by charge transfer, induces a polaronic distortion that can be rationalized in terms of compensation of surface dipoles. In fact, the local relaxation induced by the charge transfer generates a dipole moment which counteracts that due to the charge transfer, Fig. 20c and d. As a consequence, on structurally soft oxide monolayers the same adsorbed species can exist in two opposite charge states, stabilized by different displacements of the ions in the films, Fig. 20c and d.

This effect has been demonstrated for the case of Au atoms adsorbed on FeO(111)/Pt(111) ultrathin films.[241] These films exhibit a periodic variation of the interface structure due to the lattice mismatch between FeO(111) and Pt(111), with the formation of a Moiré superlattice. DFT calculations show that a Au atom deposited on FeO(111)/Pt(111) becomes negatively charged if the rumpling is locally reversed with respect to the clean surface, with an outward displacement of a Fe atom, Fig. 21a.[241] In contrast, the Au atom becomes positively charged if the oxygens relax outwards, and the Fe ions relax towards the Pt surface, Fig. 21b. Of the two configurations, charge 1− or charge 1+, only that corresponding the positively charged Au has been observed experimentally.[241] The fact that the other configuration has never been observed could be due to the presence of a kinetic barrier to reverse the local rumpling.

The same effect can be discussed with other oxides, such as MgO/Ag(100) 2 ML films, by adsorbing atoms that induce charge
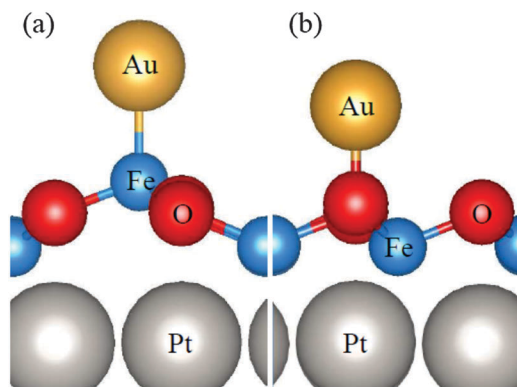

Fig. 21 Side views of a Au atom adsorbed on the FeO(111)/Pt(111) substrate: (a) flipped top-Fe configuration (negatively charged Au) and (b) direct top-O configuration (positively charged Au).
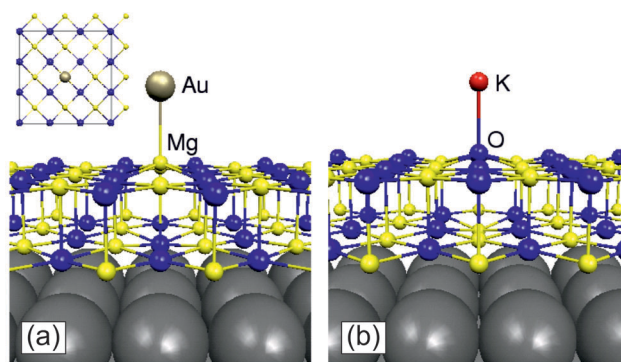

Fig. 22 Optimal geometries of (a) a Au atom adsorbed on top of a Mg cation of a MgO/Ag(100) 2 ML film and (b) a K atom adsorbed on top of an O anion of a MgO/Ag(100) 2 ML film. In both cases notice the strong relaxation of the surface ion in direct contact with the adsorbate. The inset shows a top view of the 3 × 3 supercell used in the calculations. Reproduced with permission from ref. 242. Copyright 2006 by the Royal Chemical Society.

transfer in opposite directions, such as Au and K, Fig. 22.[242] Au, negatively charged, induces an outward relaxation of the Mg ion to which it is bound, Fig. 22a. Potassium donates one electron to the support and becomes positively charged, K^+, and the surface oxide anion where K is bound relaxes outwards by 0.4 Å, Fig. 22b, while the Mg ion below it moves by 0.3 Å towards the Ag metal. Thus, adsorption of Au or K atoms leads to opposite structural relaxation of the MgO ultrathin film in order to create a surface dipole that partially screens the dipole moment generated by the charged adsorbates.

4 From model systems to real catalysts

We have seen in the previous sections how thin oxide films may be used to model specific aspects of heterogeneous catalysts by catching some of the complexity of the real powder system. In many cases lessons may be learned by experimentally testing existing hypotheses that have been used to explain observed behavior using specifically designed model systems.

This journal is © The Royal Society of Chemistry 2018

Chem. Soc. Rev., 2018, **47**, 8474–8502 | 8493

4.1 Doping

One example was the specific electron induced reactivity of carbon-dioxide and the formation of oxalate species at the rim of a Au nanoparticle supported on a thin MgO film grown on Ag.[40,202] The question is whether there is a way to transfer the knowledge gained to the design of systems closer to the reality of a powder system. In order to see the connection, let us remember that we considered the transfer of charge from the metal substrate, which led to the specific flat morphology of the Au particle and the localization of this charge at the nano-particle's rim. The energetics involve the energy necessary to release electrons from the electron source, *i.e.* the metal (Ag) support, and the electron affinity of the surface species, *i.e.* the Au particle. If we can place an electron source within the bulk of an oxide support to mimic the corresponding energetics, a similar situation should be encountered, as anticipated in Section 2.2.2.[120,159,206,243–245]

Fig. 23 shows STM images of a 60 ML thick CaO film in a (100) geometry without a Mo dopant (Fig. 23a) and with a Mo dopant (Fig. 23b).[244] Clearly, the doped material leads to an equivalent flat morphology of the Au nano-particle triggered by the electron transfer (see also Fig. 8). If a co-dopant with higher electron affinity is present, then the effect on the Au particle's morphology disappears. Fig. 23c shows the effect when Li is co-doped with Mo.[245] This example indicates how a concept developed on model systems may be directly transferred to bulk materials, as they are used in real catalysts. Of course, there are still a number of open questions as to how the dopant interacts with the Au particle on top of the surface. We infer from investigations involving not adsorbed metal nano-particles but rather molecules, such as O_2,[243] which exhibit a considerable electron affinity, and which do form anionic species on doped CaO films, that electron phonon coupling is involved in the process,[161] as discussed in Section 3.3. There is an experimental study on bulk powder material by the Schlögl group, published back to back with our conceptional work,[243,246] that hints to the validity of this.

4.2 Strong metal support interaction (SMSI)

In the Introduction the so-called Strong Metal Support Inter-action (SMSI)[25,214,219,247] was mentioned. In a reactive atmo-sphere a metal particle may be fully or partially encapsulated by
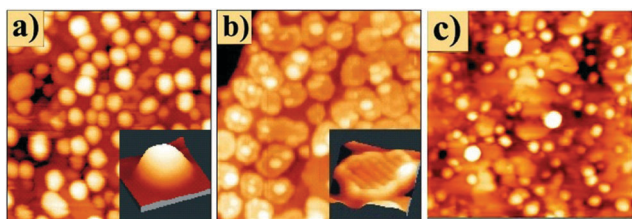

Fig. 23 STM images of 0.5 ML Au deposited onto (a) pristine CaO; (b) doped with 4% Mo; (c) doped with 4% Mo + 8% Li (6.0 V, 50 × 50 nm²).[244,245] Adapted with permission from ref. 244. Copyright 2012 by the American Physical Society. Adapted with permission from ref. 245. Copyright 2012 American Chemical Society.
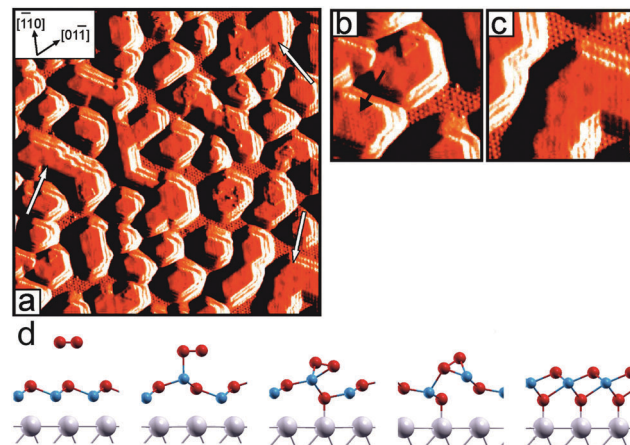

Fig. 24 STM topographic images of 3D Pt clusters (covered with a thin FeO layer after thermal treatment), where some of the descending terraces at the cluster rim are resolved. (a) STM image (scan size 80 × 80 nm², I_t = 0.6 nA, V_s = −0.5 V) of 1.8 monolayer (ML) Pt/Fe₃O₄(111) exposed to 540 Langmuir (L) at 500 K and flashed to 850 K in ultra-high vacuum (UHV). The arrows indicate some of the top facets where the Moiré superstructure is clearly observed, as enlarged in image (b). The Pt particle exhibiting a structure of about 0.6 nm periodicity is shown in image (c) (scan size 20 × 20 nm²). From ref. 214 and 257. Reprinted with permission from ref. 214. Copyright 2008 American Chemical Society. (d) Schematic representation of the transformation of an FeO bi-layer into an FeO_2 tri-layer on Pt(111) (Fe: blue, O: red, Pt: grey). Adapted with permission from ref. 257. Copyright 2010 Wiley-VCH.

a thin oxide layer, which influences the observed chemistry as compared to the pure metal. This has been often observed in real catalysis for reducible oxide supports in particular. TiO_2 is the prototypic substrate oxide for which this effect has been extensively observed and discussed.[248–251] The structure of the Ti_xO_y oxide layer over growing the metal, however, is still under debate.[213,220,252–256] Another system has therefore been chosen to attempt a deeper understanding of the way SMSI states of catalysts influence the chemistry. The particular system is Pt (and/or) Pd on magnetite. Fig. 24 shows STM images of Pt particles grown on Fe_3O_4(111) after treatment at higher temperatures, which led to the growth of an ultrathin FeO layer on top of the particles.

The STM images clearly reveal the structure of the iron oxide layer and allow us to identify it as a double Fe–O-layer, which have been previously studied extensively as grown on Pt(111) metal single crystals.[258–260] Another aspect becomes apparent, which is connected with considerations of general importance for the imaging of three-dimensional particles: imaging of the particle's perimeter is difficult, simply because the size of the tip and the geometry of the STM setup are incompatible with the task.[40] However, the structure of the films may be clearly deduced from the atomic resolution at the top facet. Since the structure of the FeO layer on the Pt particles is fully compatible with the one observed on Pt(111) single crystals, model studies have been performed on the single crystal system predominantly (although checked with parallel experiments on particles).[247] It was shown that the FeO double layer film, schematically shown in Fig. 24, transforms under oxygen rich conditions into

8494 | *Chem. Soc. Rev.*, 2018, **47**, 8474–8502

This journal is © The Royal Society of Chemistry 2018

a tri-layer film, also shown with a layer sequence of O–Fe–O/Pt as opposed to O–Fe/Pt.[261] This tri-layer exhibits considerable activity in CO oxidation at low temperature. The transformations were supported by a series of density functional calculations.[26] The structure of the tri-layer is actually not covering the entire surface, but is embedded in the bilayer FeO film.[217,262] Originally, the observed reaction was rationalized by assuming that the top oxygen layer of the tri-layer film, which is more weakly bound than the oxygen layer in the double-layer film, leads to the formation of CO_2 when exposed to CO, and the oxygen rich conditions are necessary to replenish the oxygen lost in the reaction. The situation becomes more complex, if the double-layer film does not cover the surface completely. Bao *et al.*[263] presented evidence employing UHV studies that in this case the open FeO/Pt interface is the active site for the reaction. Using additional studies,[264] including extensive STM investigations, those authors concluded that oxygen atoms, bound both to the FeO layer and to the Pt substrate, react with incoming CO to form CO_2. One has to remember that those studies were performed under UHV conditions, while the abovementioned ones under ambient conditions force the formation of the tri-layer, alluded to above. In order to evaluate the influence of the open oxide–Pt interface, studies on partially covered Pt single crystals at near atmospheric pressure were performed.[265] Indeed, the results indicated that the Pt–oxide interface is more reactive than the fully covered film.[266–271] Therefore, until recently, there has been evidence that the open oxide–metal interface (in the spirit of an inverse catalyst: see Section 3.2) is the active site. Very recently, however, experimental evidence that the most active interface under ambient conditions is not the oxide–metal interface but rather the oxide–oxide interface between the FeO double-layer and the FeO_{2-x} tri-layer has been provided.[272] Fig. 25 shows STM topographic images of iron oxide islands formed under ambient conditions. The light protrusions on the iron oxide islands represent those areas where the FeO_2 tri-layer has been formed. Panel b in Fig. 25 shows the FeO_{2-x} surface area, *i.e.* its reduction, normalized to the total island area, after exposure to CO for various times. The plot reveals first order kinetics typical for etching of two-dimensional islands from the edges.[273]

A closer look (Fig. 26) indicates that the FeO_{2-x} protrusions disappear starting from the side that is close to the overall island's rim.

The reduction thus takes place only at the interface between the "compact" FeO_2 domain and the reduced FeO surface formed *via* reduction. This is a scenario compatible with DFT calculations[265] for periodic structures, which revealed the lowest oxygen binding energy at the intrinsic FeO/FeO_{2-x} interface. If the iron oxide islands are exposed to mixtures of CO and oxygen, STM images basically corroborate the previous observation that CO/O_2 mixtures with excess CO reduce the islands and excess oxygen prevents excess reduction. However, even oxygen in large (9/1) excess does not prevent the edges (*i.e.* the metal–oxide interface) from being reduced. In order to link the structural observations to reactivity, a set of experiments using a mass spectrometer placed close to the film surface to measure
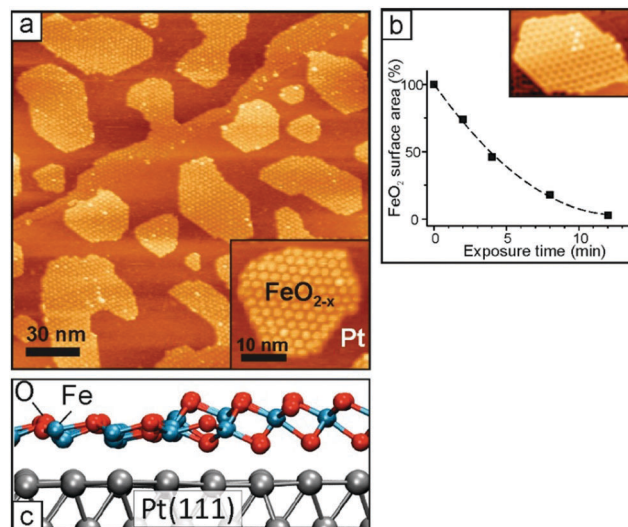

Fig. 25 (a) Typical morphology of oxidized FeO_{2-x} films on Pt(111) at submonolayer coverages. The cross-view of a $FeO_{2-x}/Pt(111)$ film is shown in the inset. (b) The FeO_{2-x} surface area normalized to the area in the "as prepared" sample as a function of the accumulative exposure time.[272] (c) Schematic based on calculations of the FeO/FeO_{2-x} interface after ref. 265. Copyright 2015 Wiley-VCH.

the amount of CO_2 produced were carried out.[272] The results obtained for a $CO/O_2:1/5$ mixture in the 10^{-6} mbar range are shown in Fig. 27.

At 450 K the reaction ignites and sustained CO_2 production (10 minutes) is observed. CO_2 formation decreases when the oxygen flow is stopped and recovers when the oxygen is readmitted, but the CO_2 production never fully recovers, in fact it decreases as the number of cycles increases. This is consistent with the idea alluded to above that even excess oxygen will not recover the metal/oxide interface but the perimeter length of the interface between the reduced FeO-like region and the FeO_{2-x} region shrinks almost linearly. Therefore, the combination of structural and activity data provides compelling evidence that the FeO/FeO_{2-x}-interface is the most active site. This result has been obtained for flat single crystals but not yet
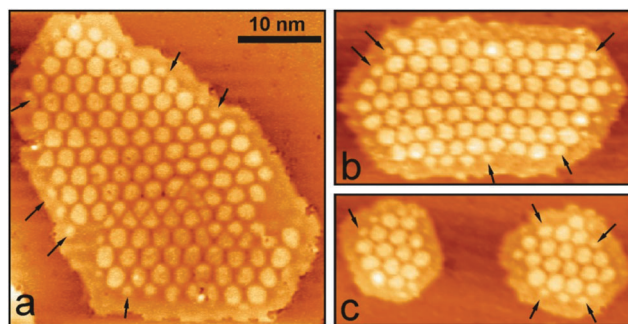

Fig. 26 STM images of the FeO_{2-x} islands after exposure to 10^{-6} mbar CO at 400 K for 4 min. Tunneling conditions: bias −3 V, current 0.05 nA. The arrows highlight non-uniform disappearance of the Moiré spots close to the island edge.[272] Reproduced with permission from ref. 272. Copyright 2015 Wiley-VCH.
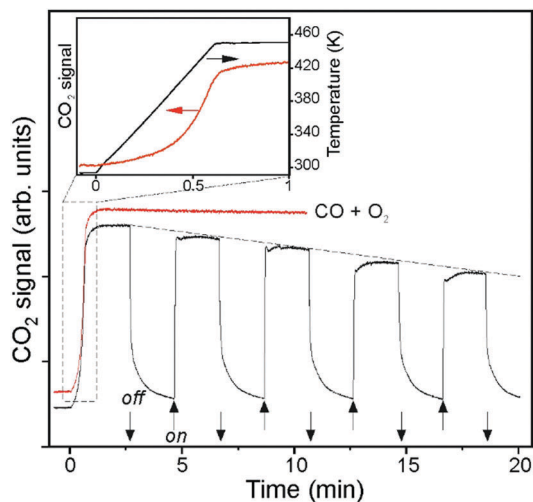
This journal is © The Royal Society of Chemistry 2018

Chem. Soc. Rev., 2018, **47**, 8474–8502 | 8495

Fig. 27 CO_2 (44 amu) signal measured by QMS in front of the sub-monolayer FeO_{2-x} film. The reaction ($CO/O_2 = 1/5$) mixture consists of 10^{-6} mbar of CO and 5×10^{-6} mbar of O_2. At time zero, the sample was heated up to the reaction temperature of 450 K with a rate of 2 K s^{-1}. The red curve shows CO_2 production under steady state conditions. The black curve shows CO_2 kinetics upon switching O_2 flow in the mixture off and on, as indicated by the arrows, while keeping the CO pressure constant.[272] Reproduced with permission from ref. 272. Copyright 2015 Wiley-VCH.

for particles. Nevertheless, given the structural similarities of the ultrathin oxide film on the single crystal and on the particles it is not unlikely that this scenario applies to the SMSI state of Pt/Fe$_3$O$_4$ under reaction conditions.

5 Epilogue

We have reviewed the state of the art in model catalysis both from a theoretical and from an experimental point of view, with particular emphasis on the exchange of charge between the oxide support and the supported metal particle. In many cases the relevant information is gained by combining theory and experiment. For this purpose it is important that both the experimentalist and the theorist try to use tools and develop model systems that can be treated with both approaches. This review covers the discussion of the concepts used, the way the systems may be prepared experimentally and controlled at the atomic level, which is a prerequisite to be able to compare directly to theory. For the latter, atomic control is part of the approach; experimentally it may be challenging sometimes. Still, the best results are obtained if efforts are made on both sides in this direction. In this review we present a number of examples where this goal has been achieved and our understanding of concepts useful for catalysis has been enriched. There are even case studies touched upon which bring model systems in direct contact with real powder catalysis. We believe that the future of more such investigations is bright.

Conflicts of interest

There are no conflicts to declare.

Acknowledgements

References

1 J. Libuda and H.-J. Freund, *Surf. Sci. Rep.*, 2005, **57**, 157–298.
2 M. Salmeron and R. Schlögl, *Surf. Sci. Rep.*, 2008, **63**, 169–199.
3 G. A. Somorjai and J. Y. Park, *Chem. Soc. Rev.*, 2008, **37**, 2155–2162.
4 A. T. Bell, *Science*, 2003, **299**, 1688–1691.
5 M. Besson, P. Gallezot and C. Pinel, *Chem. Rev.*, 2014, **114**, 1827–1870.
6 I. Chorkendorff and J. W. Niemantsverdriet, *Concepts of Modern Catalysis and Kinetics*, Wiley-VCH, 2017.
7 B. Roldan Cuenya and F. Behafarid, *Surf. Sci. Rep.*, 2015, **70**, 135–187.
8 W. P. Halperin, *Rev. Mod. Phys.*, 1986, **58**, 533–606.
9 Y. Lei, F. Mehmood, S. Lee, J. Greeley, B. Lee, S. Seifert, R. E. Winans, J. W. Elam, R. J. Meyer, P. C. Redfern, D. Teschner, R. Schlögl, M. J. Pellin, L. A. Curtiss and S. Vajda, *Science*, 2010, **328**, 224–228.
10 E. C. Tyo and S. Vajda, *Nat. Nanotechnol.*, 2015, **10**, 577.
11 R. Erni, M. D. Rossell, C. Kisielowski and U. Dahmen, *Phys. Rev. Lett.*, 2009, **102**, 096101.
12 M. A. Bañares, *Catal. Today*, 2005, **100**, 71–77.
13 A. A. Herzing, C. J. Kiely, A. F. Carley, P. Landon and G. J. Hutchings, *Science*, 2008, **321**, 1331–1335.
14 A. Chakrabarti, M. E. Ford, D. Gregory, R. Hu, C. J. Keturakis, S. Lwin, Y. Tang, Z. Yang, M. Zhu, M. A. Bañares and I. E. Wachs, *Catal. Today*, 2017, **283**, 27–53.
15 S. Tosoni and G. Pacchioni, *J. Phys. Chem. C*, 2017, **121**, 28328–28338.
16 Y. Romanyshyn, S. Guimond, H. Kuhlenbeck, S. Kaya, R. P. Blum, H. Niehus, S. Shaikhutdinov, M. Simic-Milosevic, N. Nilius, H. J. Freund, M. V. Ganduglia-Pirovano, R. Fortrie, J. Döbler and J. Sauer, *Top. Catal.*, 2008, **50**, 106–115.

8496 | *Chem. Soc. Rev.*, 2018, **47**, 8474–8502

This journal is © The Royal Society of Chemistry 2018

17 G. Pacchioni, *Phys. Chem. Chem. Phys.*, 2013, **15**, 1737–1757.

18 A. S. K. Hashmi and G. J. Hutchings, *Angew. Chem., Int. Ed.*, 2006, **45**, 7896–7936.

19 M. Haruta, *Chem. Rec.*, 2003, **3**, 75–87.

20 A. S. Wörz, U. Heiz, F. Cinquini and G. Pacchioni, *J. Phys. Chem. B*, 2005, **109**, 18418–18426.

21 A. M. Márquez, J. Graciani and J. F. Sanz, *Theor. Chem. Acc.*, 2010, **126**, 265–273.

22 E. W. McFarland and H. Metiu, *Chem. Rev.*, 2013, **113**, 4391–4427.

23 C. T. Campbell, *Nat. Chem.*, 2012, **4**, 597.

24 S. J. Tauster, S. C. Fung and R. L. Garten, *J. Am. Chem. Soc.*, 1978, **100**, 170–175.

25 S. J. Tauster, *Acc. Chem. Res.*, 1987, **20**, 389–394.

26 Y. N. Sun, L. Giordano, J. Goniakowski, M. Lewandowski, Z. H. Qin, C. Noguera, S. Shaikhutdinov, G. Pacchioni and H. J. Freund, *Angew. Chem., Int. Ed.*, 2010, **49**, 4418–4421.

27 G. M. Schwab and K. Koller, *J. Am. Chem. Soc.*, 1968, **90**, 3078–3080.

28 F. Solymosi, *Catal. Rev.: Sci. Eng.*, 1968, **1**, 233–255.

29 F. F. Vol'kenshtein, *Russ. Chem. Rev.*, 1966, **35**, 537.

30 D. W. Goodman, *Surf. Sci.*, 1994, **299–300**, 837–848.

31 H. J. Freund, *Surf. Sci.*, 2002, **500**, 271–299.

32 C. R. Henry, *Surf. Sci. Rep.*, 1998, **31**, 231–326.

33 C. Stampfl, M. Veronica Ganduglia-Pirovano, K. Reuter and M. Scheffler, *Surf. Sci.*, 2002, **500**, 368–394.

34 P. S. Bagus, F. Illas, G. Pacchioni and F. Parmigiani, *J. Electron Spectrosc. Relat. Phenom.*, 1999, **100**, 215–236.

35 Y. Zhou, J. M. Perket and J. Zhou, *J. Phys. Chem. C*, 2010, **114**, 11853–11860.

36 P. Torelli, L. Giordano, S. Benedetti, P. Luches, E. Annese, S. Valeri and G. Pacchioni, *J. Phys. Chem. C*, 2009, **113**, 19957–19965.

37 N. Nilius, M. V. Ganduglia-Pirovano, V. Brázdová, M. Kulawik, J. Sauer and H. J. Freund, *Phys. Rev. Lett.*, 2008, **100**, 096802.

38 X. Lin, N. Nilius, H. J. Freund, M. Walter, P. Frondelius, K. Honkala and H. Häkkinen, *Phys. Rev. Lett.*, 2009, **102**, 206801.

39 X. Lin, N. Nilius, M. Sterrer, P. Koskinen, H. Häkkinen and H.-J. Freund, *Phys. Rev. B: Condens. Matter Mater. Phys.*, 2010, **81**, 153406.

40 W.-D. Schneider, M. Heyde and H.-J. Freund, *Chem. – Eur. J.*, 2018, **24**, 2317–2327.

41 G. N. Vayssilov, Y. Lykhach, A. Migani, T. Staudt, G. P. Petrova, N. Tsud, T. Skála, A. Bruix, F. Illas, K. C. Prince, V. r. Matolín, K. M. Neyman and J. Libuda, *Nat. Mater.*, 2011, **10**, 310–315.

42 Y. Lykhach, S. M. Kozlov, T. Skala, A. Tovt, V. Stetsovych, N. Tsud, F. Dvorak, V. Johanek, A. Neitzel, J. Myslivecek, S. Fabris, V. Matolin, K. M. Neyman and J. Libuda, *Nat. Mater.*, 2016, **15**, 284–288.

43 D. Kong, G. Wang, Y. Pan, S. Hu, J. Hou, H. Pan, C. T. Campbell and J. Zhu, *J. Phys. Chem. C*, 2011, **115**, 6715–6725.

44 P. Luches, F. Pagliuca, S. Valeri, F. Illas, G. Preda and G. Pacchioni, *J. Phys. Chem. C*, 2012, **116**, 1122–1132.

45 V. E. Henrich and P. A. Cox, *The Surface Science of Metal Oxides*, Cambridge University Press, Cambridge, 1994.

46 P. A. Cox, *Transition Metal Oxides. An Introduction to their Electronic Structure and Properties*, Clarendon, Oxford, 1992.

47 C. T. Campbell, *Surf. Sci. Rep.*, 1997, **27**, 1–111.

48 J. Sauer, P. Ugliengo, E. Garrone and V. R. Saunders, *Chem. Rev.*, 1994, **94**, 2095–2160.

49 G. Pacchioni, J. M. Ricart and F. Illas, *J. Am. Chem. Soc.*, 1994, **116**, 10152–10158.

50 A. L. Shluger, P. V. Sushko and L. N. Kantorovich, *Phys. Rev. B: Condens. Matter Mater. Phys.*, 1999, **59**, 2417–2430.

51 M. Chiesa, E. Giamello, C. Di Valentin, G. Pacchioni, Z. Sojka and S. Van Doorslaer, *J. Am. Chem. Soc.*, 2005, **127**, 16935–16944.

52 J. C. Lian, E. Finazzi, C. Di Valentin, T. Risse, H. J. Gao, G. Pacchioni and H. J. Freund, *Chem. Phys. Lett.*, 2008, **450**, 308–311.

53 E. Finazzi, C. Di Valentin, G. Pacchioni, M. Chiesa, E. Giamello, H. Gao, J. Lian, T. Risse and H.-J. Freund, *Chem. – Eur. J.*, 2008, **14**, 4404–4414.

54 A. Ruiz Puigdollers, S. Tosoni and G. Pacchioni, *J. Phys. Chem. C*, 2016, **120**, 15329–15337.

55 A. R. Puigdollers, F. Illas and G. Pacchioni, *J. Phys. Chem. C*, 2016, **120**, 4392–4402.

56 M. Antlanger, W. Mayr-Schmölzer, J. Pavelec, F. Mittendorfer, J. Redinger, P. Varga, U. Diebold and M. Schmid, *Phys. Rev. B: Condens. Matter Mater. Phys.*, 2012, **86**, 035451.

57 H. Li, J.-I. J. Choi, W. Mayr-Schmölzer, C. Weilach, C. Rameshan, F. Mittendorfer, J. Redinger, M. Schmid and G. Rupprechter, *J. Phys. Chem. C*, 2015, **119**, 2462–2470.

58 E. Napetschnig, M. Schmid and P. Varga, *Surf. Sci.*, 2008, **602**, 1750–1756.

59 V. Maurice, M. Salmeron and G. A. Somorjai, *Surf. Sci.*, 1990, **237**, 116–126.

60 K. Meinel, A. Eichler, S. Förster, K. M. Schindler, H. Neddermeyer and W. Widdra, *Phys. Rev. B: Condens. Matter Mater. Phys.*, 2006, **74**, 235444.

61 K. Meinel, A. Eichler, K. M. Schindler and H. Neddermeyer, *Surf. Sci.*, 2004, **562**, 204–218.

62 K. Meinel, K.-M. Schindler and H. Neddermeyer, *Surf. Sci.*, 2003, **532-535**, 420–424.

63 A. Ruiz Puigdollers and G. Pacchioni, *Nanoscale*, 2017, **9**, 6866–6876.

64 J. F. Sanz and A. Márquez, *J. Phys. Chem. C*, 2007, **111**, 3949–3955.

65 Y. Han, C.-j. Liu and Q. Ge, *J. Phys. Chem. B*, 2006, **110**, 7463–7472.

66 T. Bredow, E. Aprà, M. Catti and G. Pacchioni, *Surf. Sci.*, 1998, **418**, 150–165.

67 M. A. San Miguel, C. J. Calzado and J. F. Sanz, *J. Phys. Chem. B*, 2001, **105**, 1794–1798.

68 T. Albaret, F. Finocchi, C. Noguera and A. De Vita, *Phys. Rev. B: Condens. Matter Mater. Phys.*, 2001, **65**, 035402.

69 M. Sterrer, M. Yulikov, T. Risse, H.-J. Freund, J. Carrasco, F. Illas, C. Di Valentin, L. Giordano and G. Pacchioni, *Angew. Chem., Int. Ed.*, 2006, **45**, 2633–2635.

70 C. D. Wagner, *Anal. Chem.*, 1972, **44**, 967–973.

71 C. D. Wagner, L. H. Gale and R. H. Raymond, *Anal. Chem.*, 1979, **51**, 466–482.

72 A. Bruix, K. M. Neyman and F. Illas, *J. Phys. Chem. C*, 2010, **114**, 14202–14207.

73 G. Vilé, B. Bridier, J. Wichert and J. Pérez-Ramírez, *Angew. Chem., Int. Ed.*, 2012, **51**, 8620–8623.

74 G. Vilé, S. Wrabetz, L. Floryan, M. E. Schuster, F. Girgsdies, D. Teschner and J. Pérez-Ramírez, *ChemCatChem*, 2014, **6**, 1928–1934.

75 K. Werner, X. Weng, F. Calaza, M. Sterrer, T. Kropp, J. Paier, J. Sauer, M. Wilde, K. Fukutani, S. Shaikhutdinov and H.-J. Freund, *J. Am. Chem. Soc.*, 2017, **139**, 17608–17616.

76 M. Wilde and K. Fukutani, *Surf. Sci. Rep.*, 2014, **69**, 196–295.

77 H. L. Tuller and S. R. Bishop, *Annu. Rev. Mater. Res.*, 2011, **41**, 369–398.

78 P. Baranek, G. Pinarello, C. Pisani and R. Dovesi, *Phys. Chem. Chem. Phys.*, 2000, **2**, 3893–3901.

79 A. M. Ferrari and G. Pacchioni, *J. Phys. Chem.*, 1995, **99**, 17010–17018.

80 J. Kramer, W. Ernst, C. Tegenkamp and H. Pfnür, *Surf. Sci.*, 2002, **517**, 87–97.

81 L. N. Kantorovich, J. M. Holender and M. J. Gillan, *Surf. Sci.*, 1995, **343**, 221–239.

82 E. Scorza, U. Birkenheuer and C. Pisani, *J. Chem. Phys.*, 1997, **107**, 9645–9658.

83 L. Ojamäe and C. Pisani, *J. Chem. Phys.*, 1998, **109**, 10984–10995.

84 O. Diwald, M. Sterrer and E. Knozinger, *Phys. Chem. Chem. Phys.*, 2002, **4**, 2811–2817.

85 M. Ulmann, N. R. De Tacconi and J. Augustynski, *J. Phys. Chem.*, 1986, **90**, 6523–6530.

86 D. Chen, C. Chen, Z. M. Baiyee, Z. Shao and F. Ciucci, *Chem. Rev.*, 2015, **115**, 9869–9921.

87 M. Chiesa, F. Napoli and E. Giamello, *J. Phys. Chem. C*, 2007, **111**, 5481–5485.

88 F. Napoli, M. Chiesa, E. Giamello, E. Finazzi, C. Di Valentin and G. Pacchioni, *J. Am. Chem. Soc.*, 2007, **129**, 10575–10581.

89 S. A. Chambers, T. Droubay, D. R. Jennison and T. R. Mattsson, *Science*, 2002, **297**, 827–831.

90 D. Ricci, C. Di Valentin, G. Pacchioni, P. V. Sushko, A. L. Shluger and E. Giamello, *J. Am. Chem. Soc.*, 2003, **125**, 738–747.

91 M. Chiesa, M. C. Paganini, E. Giamello, C. Di Valentin and G. Pacchioni, *Angew. Chem., Int. Ed.*, 2003, **42**, 1759–1761.

92 M. Chiesa, M. C. Paganini, E. Giamello, D. M. Murphy, C. Di Valentin and G. Pacchioni, *Acc. Chem. Res.*, 2006, **39**, 861–867.

93 F. Napoli, M. Chiesa, E. Giamello, E. Finazzi, C. Di Valentin and G. Pacchioni, *J. Am. Chem. Soc.*, 2007, **129**, 10575–10581.

94 K. P. McKenna and A. Shluger, *Nat. Mater.*, 2008, **7**, 859–862.

95 X. Lin, B. Yang, H. M. Benia, P. Myrach, M. Yulikov, A. Aumer, M. Brown, M. Sterrer, O. Bondarchuk, E. Kieseritzky, J. Rocker, T. Risse, H. Gao, N. Nilius and H. J. Freund, *J. Am. Chem. Soc.*, 2010, **132**, 7745–7749.

96 G. Pacchioni, *ChemPhysChem*, 2003, **4**, 1041–1047.

97 G. Stapper, M. Bernasconi, N. Nicoloso and M. Parrinello, *Phys. Rev. B: Condens. Matter Mater. Phys.*, 1999, **59**, 797–810.

98 G. Pacchioni and G. Ieranò, *Phys. Rev. Lett.*, 1997, **79**, 753–756.

99 C. Di Valentin, G. Pacchioni and A. Selloni, *Phys. Rev. Lett.*, 2006, **97**, 166803.

100 A. Migani, G. N. Vayssilov, S. T. Bromley, F. Illas and K. M. Neyman, *J. Mater. Chem.*, 2010, **20**, 10535–10546.

101 J.-F. Jerratsch, X. Shao, N. Nilius, H.-J. Freund, C. Popa, M. V. Ganduglia-Pirovano, A. M. Burow and J. Sauer, *Phys. Rev. Lett.*, 2011, **106**, 246801.

102 L. Giordano, C. Di Valentin, J. Goniakowski and G. Pacchioni, *Phys. Rev. Lett.*, 2004, **92**, 096105.

103 A. Bogicevic and D. R. Jennison, *Surf. Sci.*, 2002, **515**, L481–L486.

104 T. König, G. H. Simon, U. Martinez, L. Giordano, G. Pacchioni, M. Heyde and H.-J. Freund, *ACS Nano*, 2010, **4**, 2510–2514.

105 A. Del Vitto, L. Giordano, G. Pacchioni and N. Rösch, *Surf. Sci.*, 2005, **575**, 103–114.

106 M. Sterrer, M. Yulikov, E. Fischbach, M. Heyde, H.-P. Rust, G. Pacchioni, T. Risse and H.-J. Freund, *Angew. Chem., Int. Ed.*, 2006, **45**, 2630–2632.

107 S. Fabris, G. Vicario, G. Balducci, S. de Gironcoli and S. Baroni, *J. Phys. Chem. B*, 2005, **109**, 22860–22867.

108 E. Wuilloud, B. Delley, W. D. Schneider and Y. Baer, *Phys. Rev. Lett.*, 1984, **53**, 202–205.

109 N. A. Deskins and M. Dupuis, *Phys. Rev. B: Condens. Matter Mater. Phys.*, 2007, **75**, 195212.

110 I. Bannat, K. Wessels, T. Oekermann, J. Rathousky, D. Bahnemann and M. Wark, *Chem. Mater.*, 2009, **21**, 1645–1653.

111 X.-Q. Gong, A. Selloni, O. Dulub, P. Jacobson and U. Diebold, *J. Am. Chem. Soc.*, 2008, **130**, 370–381.

112 Z. Hu, B. Li, X. Sun and H. Metiu, *J. Phys. Chem. C*, 2011, **115**, 3065–3074.

113 V. Shapovalov and H. Metiu, *J. Catal.*, 2007, **245**, 205–214.

114 N. Mammen, S. Narasimhan and S. d. Gironcoli, *J. Am. Chem. Soc.*, 2011, **133**, 2801–2803.

115 X. Shao, S. Prada, L. Giordano, G. Pacchioni, N. Nilius and H.-J. Freund, *Angew. Chem., Int. Ed.*, 2011, **50**, 11525–11527.

116 M. Bäumer and H.-J. Freund, *Prog. Surf. Sci.*, 1999, **61**, 127–198.

117 X. Lai, T. P. S. Clair, M. Valden and D. W. Goodman, *Prog. Surf. Sci.*, 1998, **59**, 25–52.

118 D. Ricci, A. Bongiorno, G. Pacchioni and U. Landman, *Phys. Rev. Lett.*, 2006, **97**, 036106.

119 M. Sterrer, T. Risse, M. Heyde, H.-P. Rust and H.-J. Freund, *Phys. Rev. Lett.*, 2007, **98**, 206103.

120 F. Stavale, X. Shao, N. Nilius, H.-J. Freund, S. Prada, L. Giordano and G. Pacchioni, *J. Am. Chem. Soc.*, 2012, **134**, 11380–11383.

121 M. Xu, T. Liang, M. Shi and H. Chen, *Chem. Rev.*, 2013, **113**, 3766–3798.

122 M. Osada and T. Sasaki, *Adv. Mater.*, 2012, **24**, 210–228.

123 G. Pacchioni, *Chem. – Eur. J.*, 2012, **18**, 10144–10158.

8498 | *Chem. Soc. Rev.*, 2018, **47**, 8474–8502

This journal is © The Royal Society of Chemistry 2018

124 E. P. Gusev, in *Defects in SiO₂ and Related Dielectrics: Science and Technology*, ed. G. Pacchioni, L. Skuja and D. L. Griscom, Springer Netherlands, Dordrecht, 2000, pp. 557–579, DOI: 10.1007/978-94-010-0944-7_21.

125 C. O. A. Olsson and D. Landolt, *Electrochim. Acta*, 2003, **48**, 1093–1104.

126 D. Costa, T. Ribeiro, F. Mercuri, G. Pacchioni and P. Marcus, *Adv. Mater. Interfaces*, 2014, **1**, 1300072.

127 C. H. Ahn, K. M. Rabe and J.-M. Triscone, *Science*, 2004, **303**, 488–491.

128 C. G. Granqvist, *Sol. Energy Mater. Sol. Cells*, 2007, **91**, 1529–1598.

129 S. S. P. Parkin, C. Kaiser, A. Panchula, P. M. Rice, B. Hughes, M. Samant and S.-H. Yang, *Nat. Mater.*, 2004, **3**, 862–867.

130 *Oxide Ultrathin Films: Science and Technology*, ed. G. Pacchioni and S. Valeri, Wiley-VCH, Weinheim, 2012.

131 X. Xu and D. W. Goodman, *Appl. Phys. Lett.*, 1992, **61**, 774–776.

132 H. J. Freund, H. Kuhlenbeck and V. Staemmler, *Rep. Prog. Phys.*, 1996, **59**, 283–347.

133 H.-J. Freund and G. Pacchioni, *Chem. Soc. Rev.*, 2008, **37**, 2224–2242.

134 S. Surnev, M. G. Ramsey and F. P. Netzer, *Prog. Surf. Sci.*, 2003, **73**, 117–165.

135 Q.-H. Wu, A. Fortunelli and G. Granozzi, *Int. Rev. Phys. Chem.*, 2009, **28**, 517–576.

136 L. Giordano and G. Pacchioni, *Acc. Chem. Res.*, 2011, **44**, 1244–1252.

137 G. Pacchioni and H.-J. Freund, *Chem. Rev.*, 2013, **113**, 4035–4072.

138 M. Frank, M. Bäumer, R. Kühnemuth and H.-J. Freund, *J. Phys. Chem. B*, 2001, **105**, 8569–8576.

139 S. C. Street and D. W. Goodman, in *Growth and Properties of Ultrathin Epitaxial Layers, The Chemical Physics of Solid Surfaces*, ed. D. A. King and D. P. Woodruff, Elsevier, New York, 1997, vol. 8, p. 375.

140 U. Heiz, F. Vanolli, L. Trento and W. D. Schneider, *Rev. Sci. Instrum.*, 1997, **68**, 1986.

141 M. C. Wu, J. S. Corneille, C. A. Estrada, J.-W. He and D. W. Goodman, *Chem. Phys. Lett.*, 1991, **182**, 472–478.

142 M. C. Wu, J. S. Corneille, J. W. He, C. A. Estrada and D. W. Goodman, *J. Vac. Sci. Technol., A*, 1992, **10**, 1467–1471.

143 X. Shao, P. Myrach, N. Nilius and H.-J. Freund, *J. Phys. Chem. C*, 2011, **115**, 8784.

144 M. Liehr, P. A. Thiry, J. J. Pireaux and R. Caudano, *Phys. Rev. B: Condens. Matter Mater. Phys.*, 1986, **33**, 5682–5697.

145 L. H. Tjeng, A. R. Vos and G. A. Sawatzky, *Surf. Sci.*, 1990, **235**, 269–279.

146 J.-W. He and P. J. Møller, *Surf. Sci.*, 1986, **178**, 934–942.

147 J.-W. He and P. J. Møller, *Surf. Sci.*, 1987, **180**, 411–420.

148 I. Alstrup and P. J. Møller, *Appl. Surf. Sci.*, 1988, **33–34**, 143–151.

149 S. Schintke, S. Messerli, M. Pivetta, F. Patthey, L. Libioulle, M. Stengel, A. De Vita and W.-D. Schneider, *Phys. Rev. Lett.*, 2001, **87**, 2768011.

150 J. Pal, M. Smerieri, E. Celasco, L. Savio, L. Vattuone and M. Rocca, *Phys. Rev. Lett.*, 2014, **112**, 126102.

151 R. G. S. Pala and H. Metiu, *J. Phys. Chem. C*, 2007, **111**, 12715–12722.

152 S. Baumann, I. G. Rau, S. Loth, C. P. Lutz and A. J. Heinrich, *ACS Nano*, 2014, **8**, 1739–1744.

153 K. P. McKenna and A. L. Shluger, *Phys. Rev. B: Condens. Matter Mater. Phys.*, 2009, **79**, 224116.

154 H. M. Benia, P. Myrach, A. Gonchar, T. Risse, M. Nilius and H. J. Freund, *Phys. Rev. B: Condens. Matter Mater. Phys.*, 2010, **81**, 241415.

155 S. Stuckenholz, C. Büchner, M. Heyde and H.-J. Freund, *J. Phys. Chem. C*, 2015, **119**, 12283–12290.

156 T. König, G. H. Simon, H. P. Rust, G. Pacchioni, M. Heyde and H. J. Freund, *J. Am. Chem. Soc.*, 2009, **131**, 17544–17545.

157 M. Heyde, G. H. Simon, H.-P. Rust and H.-J. Freund, *Appl. Phys. Lett.*, 2006, **89**, 263107.

158 S. Schintke and W. D. Schneider, *J. Phys.: Condens. Matter*, 2004, **16**, R49.

159 Y. Cui, X. Shao, S. Prada, L. Giordano, G. Pacchioni, H.-J. Freund and N. Nilius, *Phys. Chem. Chem. Phys.*, 2014, **16**, 12764–12772.

160 Y. Cui, Y. Pan, L. Pascua, H. Qiu, C. Stiehler, H. Kuhlenbeck, N. Nilius and H.-J. Freund, *Phys. Rev. B: Condens. Matter Mater. Phys.*, 2015, **91**, 035418.

161 Y. Cui, S. Tosoni, W.-D. Schneider, G. Pacchioni, N. Nilius and H.-J. Freund, *Phys. Rev. Lett.*, 2015, **114**, 016804.

162 H.-J. Freund, *Acc. Chem. Res.*, 2017, **50**, 446–449.

163 C. Büchner, L. Lichtenstein, X. Yu, J. A. Boscoboinik, B. Yang, W. E. Kaden, M. Heyde, S. K. Shaikhutdinov, R. Włodarczyk, M. Sierka, J. Sauer and H.-J. Freund, *Chem. – Eur. J.*, 2014, **20**, 9176–9183.

164 X. Yu, B. Yang, J. A. Boscoboinik, S. Shaikhutdinov and H.-J. Freund, *Appl. Phys. Lett.*, 2012, **100**, 151608.

165 M. Heyde, S. Shaikhutdinov and H.-J. Freund, *Chem. Phys. Lett.*, 2012, **550**, 1–7.

166 L. Lichtenstein, M. Heyde and H.-J. Freund, *J. Phys. Chem. C*, 2012, **116**, 20426–20432.

167 L. Lichtenstein, C. Büchner, B. Yang, S. Shaikhutdinov, M. Heyde, M. Sierka, R. Włodarczyk, J. Sauer and H.-J. Freund, *Angew. Chem., Int. Ed.*, 2012, **51**, 404–407.

168 W. H. Zachariasen, *J. Am. Chem. Soc.*, 1932, **54**, 3841–3851.

169 J. P. Hogan, *J. Polym. Sci., Part A: Polym. Chem.*, 1970, **8**, 2637–2652.

170 E. Groppo, C. Lamberti, S. Bordiga, G. Spoto and A. Zecchina, *Chem. Rev.*, 2005, **105**, 115–184.

171 B. M. Weckhuysen, R. A. Schoonheydt, J. M. Jehng, I. E. Wachs, S. J. Cho, R. Ryoo, S. Kijlstra and E. Poels, *J. Chem. Soc., Faraday Trans.*, 1995, **91**, 3245–3253.

172 M. P. McDaniel, in *Advances in Catalysis*, ed. C. G. Bruce and K. Helmut, Academic Press, 2010, vol. 53, pp. 123–606.

173 C. Brown, J. Krzystek, R. Achey, A. Lita, R. Fu, R. W. Meulenberg, M. Polinski, N. Peek, Y. Wang, L. J. van de Burgt, S. Profeta, A. E. Stiegman and S. L. Scott, *ACS Catal.*, 2015, **5**, 5574–5583.

This journal is © The Royal Society of Chemistry 2018

Chem. Soc. Rev., 2018, **47**, 8474–8502 | 8499

174 E. Groppo, C. Lamberti, S. Bordiga, G. Spoto and A. Zecchina, *J. Catal.*, 2006, **240**, 172–181.

175 E. L. Lee and I. E. Wachs, *J. Phys. Chem. C*, 2007, **111**, 14410–14425.

176 M. P. Conley, M. F. Delley, G. Siddiqi, G. Lapadula, S. Norsic, V. Monteil, O. V. Safonova and C. Copéret, *Angew. Chem., Int. Ed.*, 2014, **53**, 1872–1876.

177 M. F. Delley, F. Núñez-Zarur, M. P. Conley, A. Comas-Vives, G. Siddiqi, S. Norsic, V. Monteil, O. V. Safonova and C. Copéret, *Proc. Natl. Acad. Sci. U. S. A.*, 2014, **111**, 11624–11629.

178 P. C. Thüne, J. Loos, A. M. de Jong, P. J. Lemstra and J. W. Niemantsverdriet, *Top. Catal.*, 2000, **13**, 67–74.

179 P. C. Thüne, J. Loos, X. Chen, E. M. E. van Kimmenade, B. Kong and J. W. Niemantsverdriet, *Top. Catal.*, 2007, **46**, 239–245.

180 Q. Pan, L. Li, S. Shaikhutdinov and H.-J. Freund, *J. Catal.*, 2018, **357**, 12–19.

181 Q. Pan, L. Li, S. Shaikhutdinov, Y. Fujimori, M. Hollerer, M. Sterrer and H.-J. Freund, *Faraday Discuss.*, 2017, DOI: 10.1039/C7FD00209B.

182 X. Yu, E. Emmez, Q. Pan, B. Yang, S. Pomp, W. E. Kaden, M. Sterrer, S. Shaikhutdinov, H.-J. Freund, I. Goikoetxea, R. Wlodarczyk and J. Sauer, *Phys. Chem. Chem. Phys.*, 2016, **18**, 3755–3764.

183 B. Yang, E. Emmez, W. E. Kaden, X. Yu, J. A. Boscoboinik, M. Sterrer, S. Shaikhutdinov and H. J. Freund, *J. Phys. Chem. C*, 2013, **117**, 8336–8344.

184 M. Sterrer and H.-J. Freund, *Catal. Lett.*, 2013, **143**, 375–385.

185 J. Libuda, M. Frank, A. Sandell, S. Andersson, P. A. Brühwiler, M. Bäumer, N. Mårtensson and H. J. Freund, *Surf. Sci.*, 1997, **384**, 106–119.

186 M. Frank, M. Bäumer, R. Kuehnemuth and H. J. Freund, *J. Phys. Chem. B*, 2001, **105**, 8569.

187 U. Heiz and W. D. Schneider, *Crit. Rev. Solid State Mater. Sci.*, 2001, **26**, 251–290.

188 P. Fayet, F. Granzer, G. Hegenbart, E. Moisar, B. Pischel and L. Wöste, *Phys. Rev. Lett.*, 1985, **55**, 3002–3004.

189 N. Nilius, T. M. Wallis and W. Ho, *Phys. Rev. Lett.*, 2003, **90**, 046808.

190 A. Bogicevic and D. R. Jennison, *Phys. Rev. Lett.*, 1999, **82**, 4050.

191 K. M. Neyman, S. Vent, N. Rösch and G. Pacchioni, *Top. Catal.*, 1999, **9**, 153–161.

192 J. Repp, G. Meyer, F. E. Olsson and M. Persson, *Science*, 2004, **305**, 493–495.

193 F. E. Olsson, S. Paavilainen, M. Persson, J. Repp and G. Meyer, *Phys. Rev. Lett.*, 2007, **98**, 176803.

194 G. Pacchioni, L. Giordano and M. Baistrocchi, *Phys. Rev. Lett.*, 2005, **94**, 226104.

195 M. Sterrer, T. Risse, U. Martinez Pozzoni, L. Giordano, M. Heyde, H.-P. Rust, G. Pacchioni and H.-J. Freund, *Phys. Rev. Lett.*, 2007, **98**, 096107.

196 C. D. Wagner, *Faraday Discuss. Chem. Soc.*, 1975, **60**, 291–300.

197 P. S. Bagus, A. Wieckowski and H. Freund, *Chem. Phys. Lett.*, 2006, **420**, 42–46.

198 R. N. Sodhi and R. G. Cavell, *J. Electron Spectrosc. Relat. Phenom.*, 1983, **32**, 283–312.

199 G. Hohlneicher, H. Pulm and H.-J. Freund, *J. Electron Spectrosc. Relat. Phenom.*, 1985, **37**, 209–224.

200 W. E. Kaden, C. Büchner, L. Lichtenstein, S. Stuckenholz, F. Ringleb, M. Heyde, M. Sterrer, H.-J. Freund, L. Giordano, G. Pacchioni, C. J. Nelin and P. S. Bagus, *Phys. Rev. B: Condens. Matter Mater. Phys.*, 2014, **89**, 115436.

201 C. P. O'Brien, K. H. Dostert, M. Hollerer, C. Stiehler, F. Calaza, S. Schauermann, S. Shaikhutdinov, M. Sterrer and H. J. Freund, *Faraday Discuss.*, 2016, **188**, 309–321.

202 F. Calaza, C. Stiehler, Y. Fujimori, M. Sterrer, S. Beeg, M. Ruiz-Oses, N. Nilius, M. Heyde, T. Parviainen, K. Honkala, H. Häkkinen and H.-J. Freund, *Angew. Chem., Int. Ed.*, 2015, **54**, 12484–12487.

203 A. Stamatovic, K. Stephan and T. D. Märk, *Int. J. Mass Spectrom. Ion Processes*, 1985, **63**, 37–47.

204 R. N. Compton, P. W. Reinhardt and C. D. Cooper, *J. Chem. Phys.*, 1975, **63**, 3821–3827.

205 F. M. Hoffmann, M. D. Weisel and J. A. K. Paul, *Carbon Dioxide Chemistry*, Woodhead Publishing, 1994, pp. 55–63, DOI: 10.1016/B978-1-85573-799-0.50011-X.

206 Y. Cui, C. Stiehler, N. Nilius and H.-J. Freund, *Phys. Rev. B: Condens. Matter Mater. Phys.*, 2015, **92**, 075444.

207 X. Shao, Y. Cui, W.-D. Schneider, N. Nilius and H.-J. Freund, *J. Phys. Chem. C*, 2012, **116**, 17980–17984.

208 H.-J. Freund, *J. Am. Chem. Soc.*, 2016, **138**, 8985–8996.

209 Y. Martynova, B. H. Liu, M. E. McBriarty, I. M. N. Groot, M. J. Bedzyk, S. Shaikhutdinov and H. J. Freund, *J. Catal.*, 2013, **301**, 227–232.

210 I. X. Green, W. J. Tang, M. Neurock and J. T. Yates, *Science*, 2011, **333**, 736–739.

211 J. A. Rodriguez, S. Ma, P. Liu, J. Hrbek, J. Evans and M. Pérez, *Science*, 2007, **318**, 1757–1760.

212 K. Hayek, M. Fuchs, B. Klötzer, W. Reichl and G. Rupprechter, *Top. Catal.*, 2000, **13**, 55–66.

213 M. Bowker, P. Stone, P. Morrall, R. Smith, R. Bennett, N. Perkins, R. Kvon, C. Pang, E. Fourre and M. Hall, *J. Catal.*, 2005, **234**, 172–181.

214 Z. H. Qin, M. Lewandowski, Y. N. Sun, S. Shaikhutdinov and H. J. Freund, *J. Phys. Chem. C*, 2008, **112**, 10209–10213.

215 Y.-N. Sun, Z.-H. Qin, M. Lewandowski, S. Kaya, S. Shaikhutdinov and H.-J. Freund, *Catal. Lett.*, 2008, **126**, 31–35.

216 Y. Lei, M. Lewandowski, Y.-N. Sun, Y. Fujimori, Y. Martynova, I. M. N. Groot, R. J. Meyer, L. Giordano, G. Pacchioni, J. Goniakowski, C. Noguera, S. Shaikhutdinov and H.-J. Freund, *ChemCatChem*, 2011, **3**, 671–674.

217 L. Giordano, M. Lewandowski, I. M. N. Groot, Y. N. Sun, J. Goniakowski, C. Noguera, S. Shaikhutdinov, G. Pacchioni and H. J. Freund, *J. Phys. Chem. C*, 2010, **114**, 21504–21509.

218 M. Lewandowski, Y. N. Sun, Z. H. Qin, S. Shaikhutdinov and H. J. Freund, *Appl. Catal., A*, 2011, **391**, 407–410.

219 M. G. Willinger, W. Zhang, O. Bondarchuk, S. Shaikhutdinov, H.-J. Freund and R. Schlögl, *Angew. Chem., Int. Ed.*, 2014, **53**, 5998–6001.

8500 | *Chem. Soc. Rev.*, 2018, **47**, 8474–8502

This journal is © The Royal Society of Chemistry 2018

220 O. Dulub, W. Hebenstreit and U. Diebold, *Phys. Rev. Lett.*, 2000, **84**, 3646–3649.

221 S. Helveg, J. V. Lauritsen, E. Lægsgaard, I. Stensgaard, J. K. Nørskov, B. S. Clausen, H. Topsøe and F. Besenbacher, *Phys. Rev. Lett.*, 2000, **84**, 951–954.

222 M. V. Bollinger, J. V. Lauritsen, K. W. Jacobsen, J. K. Nørskov, S. Helveg and F. Besenbacher, *Phys. Rev. Lett.*, 2001, **87**, 196803.

223 L. Giordano, M. Baistrocchi and G. Pacchioni, *Phys. Rev. B: Condens. Matter Mater. Phys.*, 2005, **72**, 115403.

224 A. Hellman, S. Klacar and H. Grönbeck, *J. Am. Chem. Soc.*, 2009, **131**, 16636–16637.

225 A. Gonchar, T. Risse, H.-J. Freund, L. Giordano, C. Di Valentin and G. Pacchioni, *Angew. Chem., Int. Ed.*, 2011, **50**, 2635–2638.

226 G. Pacchioni, A. M. Ferrari and E. Giamello, *Chem. Phys. Lett.*, 1996, **255**, 58–64.

227 M. Chiesa, E. Giamello, M. C. Paganini, Z. Sojka and D. M. Murphy, *J. Chem. Phys.*, 2002, **116**, 4266–4274.

228 F. Napoli, M. Chiesa, E. Giamello, G. Preda, C. Di Valentin and G. Pacchioni, *Chem. – Eur. J.*, 2010, **16**, 6776–6785.

229 C. J. Nelin, P. S. Bagus, M. A. Brown, M. Sterrer and H.-J. Freund, *Angew. Chem., Int. Ed.*, 2011, **50**, 10174–10177.

230 J. Weissenrieder, S. Kaya, J.-L. Lu, H.-J. Gao, S. Shaikhutdinov, H.-J. Freund, M. Sierka, T. K. Todorova and J. Sauer, *Phys. Rev. Lett.*, 2005, **95**, 076103.

231 L. Giordano, D. Ricci, G. Pacchioni and P. Ugliengo, *Surf. Sci.*, 2005, **584**, 225–236.

232 J. L. Lu, S. Kaya, J. Weissenrieder, H. J. Gao, S. Shaikhutdinov and H. J. Freund, *Surf. Sci.*, 2006, **600**, L153–L157.

233 S. Ulrich, N. Nilius, H.-J. Freund, U. Martinez, L. Giordano and G. Pacchioni, *ChemPhysChem*, 2008, **9**, 1367–1370.

234 S. Ulrich, N. Nilius, H.-J. Freund, U. Martinez, L. Giordano and G. Pacchioni, *Surf. Sci.*, 2009, **603**, 1145–1149.

235 U. Martinez, J.-F. Jerratsch, N. Nilius, L. Giordano, G. Pacchioni and H.-J. Freund, *Phys. Rev. Lett.*, 2009, **103**, 056801.

236 J. F. Jerratsch, N. Nilius, H.-J. Freund, U. Martinez, L. Giordano and G. Pacchioni, *Phys. Rev. B: Condens. Matter Mater. Phys.*, 2009, **80**, 245423.

237 U. Martinez, L. Giordano and G. Pacchioni, *ChemPhysChem*, 2010, **11**, 412–418.

238 J. Goniakowski, C. Noguera and L. Giordano, *Phys. Rev. Lett.*, 2007, **98**, 205701.

239 J. Goniakowski and C. Noguera, *Phys. Rev. B: Condens. Matter Mater. Phys.*, 2009, **79**, 155433.

240 J. Goniakowski, C. Noguera, L. Giordano and G. Pacchioni, *Phys. Rev. B: Condens. Matter Mater. Phys.*, 2009, **80**, 125403.

241 L. Giordano, G. Pacchioni, J. Goniakowski, N. Nilius, E. D. L. Rienks and H.-J. Freund, *Phys. Rev. Lett.*, 2008, **101**, 026102.

242 L. Giordano and G. Pacchioni, *Phys. Chem. Chem. Phys.*, 2006, **8**, 3335–3341.

243 Y. Cui, X. Shao, M. Baldofski, J. Sauer, N. Nilius and H.-J. Freund, *Angew. Chem., Int. Ed.*, 2013, **52**, 11385–11387.

244 X. Shao, N. Nilius and H.-J. Freund, *Phys. Rev. B: Condens. Matter Mater. Phys.*, 2012, **85**, 115444.

245 X. Shao, N. Nilius and H.-J. Freund, *J. Am. Chem. Soc.*, 2012, **134**, 2532–2534.

246 P. Schwach, M. G. Willinger, A. Trunschke and R. Schlögl, *Angew. Chem., Int. Ed.*, 2013, **52**, 11381–11384.

247 K. Zhang, S. Shaikhutdinov and H.-J. Freund, *ChemCatChem*, 2015, **7**, 3725–3730.

248 F. Pesty, H.-P. Steinrück and T. E. Madey, *Surf. Sci.*, 1995, **339**, 83–95.

249 J.-M. Pan and T. E. Madey, *Catal. Lett.*, 1993, **20**, 269–274.

250 F. Cosandey, L. Zhang and T. E. Madey, *Surf. Sci.*, 2001, **474**, 1–13.

251 T. Suzuki and R. Souda, *Surf. Sci.*, 2000, **448**, 33–39.

252 D. R. Jennison, O. Dulub, W. Hebenstreit and U. Diebold, *Surf. Sci.*, 2001, **492**, L677–L687.

253 R. A. Bennett, P. Stone and M. Bowker, *Catal. Lett.*, 1999, **59**, 99–105.

254 M. Bowker, P. Stone, R. Bennett and N. Perkins, *Surf. Sci.*, 2002, **497**, 155–165.

255 F. Silly and M. R. Castell, *J. Phys. Chem. B*, 2005, **109**, 12316–12319.

256 F. Sedona, S. Agnoli and G. Granozzi, *J. Phys. Chem. B*, 2006, **110**, 15359–15367.

257 Y.-N. Sun, L. Giordano, J. Goniakowski, M. Lewandowski, Z.-H. Qin, C. Noguera, S. Shaikhutdinov, G. Pacchioni and H.-J. Freund, *Angew. Chem., Int. Ed.*, 2010, **49**, 4418–4421.

258 G. H. Vurens, M. Salmeron and G. A. Somorjai, *Surf. Sci.*, 1988, **201**, 129.

259 L. Giordano, G. Pacchioni, J. Goniakowski, N. Nilius, E. D. L. Rienks and H.-J. Freund, *Phys. Rev. B: Condens. Matter Mater. Phys.*, 2007, **76**, 075416.

260 L. R. Merte, J. Knudsen, L. C. Grabow, R. T. Vang, E. Lægsgaard, M. Mavrikakis and F. Besenbacher, *Surf. Sci.*, 2009, **603**, L15–L18.

261 Y. N. Sun, Z. H. Qin, M. Lewandowski, E. Carrasco, M. Sterrer, S. Shaikhutdinov and H. J. Freund, *J. Catal.*, 2009, **266**, 359–368.

262 L. R. Merte, Y. Bai, H. Zeuthen, G. Peng, L. Lammich, F. Besenbacher, M. Mavrikakis and S. Wendt, *Surf. Sci.*, 2016, **652**, 261–268.

263 Q. Fu, W.-X. Li, Y. Yao, L. Hongyang, Q. Fu, H.-Y. Su, D. Ma, X.-K. Gu, L. Chen, Z. Wang, H. Zhang, B. Wang and X. Bao, *Science*, 2010, **328**, 1141–1144.

264 D. Sun, X.-K. Gu, R. Ouyang, H.-Y. Su, Q. Fu, X. Bao and W.-X. Li, *J. Phys. Chem. C*, 2012, **116**, 7491–7498.

265 Q. Pan, X. Weng, M. S. Chen, L. Giordano, G. Pacchioni, C. Noguera, J. Goniakowski, S. Shaikhutdinov and H.-J. Freund, *ChemCatChem*, 2015, **7**, 2620–2627.

266 L. R. Merte, C. J. Heard, F. Zhang, J. Choi, M. Shipilin, J. Gustafson, J. F. Weaver, H. Grönbeck and E. Lundgren, *Angew. Chem., Int. Ed.*, 2016, **55**, 9267–9271.

267 N. Johansson, L. R. Merte, E. Grånäs, S. Wendt, J. N. Andersen, J. Schnadt and J. Knudsen, *Top. Catal.*, 2016, **59**, 506–515.

This journal is © The Royal Society of Chemistry 2018

Chem. Soc. Rev., 2018, **47**, 8474–8502 | 8501

268 H. Chen, Y. Liu, F. Yang, M. Wei, X. Zhao, Y. Ning, Q. Liu, Y. Zhang, Q. Fu and X. Bao, *J. Phys. Chem. C*, 2017, **121**, 10398–10405.

269 Y. Liu, F. Yang, Y. Zhang, J. Xiao, L. Yu, Q. Liu, Y. Ning, Z. Zhou, H. Chen, W. Huang, P. Liu and X. Bao, *Nat. Commun.*, 2017, **8**, 14459.

270 Q. Fu, Y. Yao, X. Guo, M. Wei, Y. Ning, H. Liu, F. Yang, Z. Liu and X. Bao, *Phys. Chem. Chem. Phys.*, 2013, **15**, 14708–14714.

271 W. Kudernatsch, G. Peng, H. Zeuthen, Y. Bai, L. R. Merte, L. Lammich, F. Besenbacher, M. Mavrikakis and S. Wendt, *ACS Nano*, 2015, **9**, 7804–7814.

272 K. Zhang, L. Li, S. Shaikhutdinov and H.-J. Freund, *Angew. Chem., Int. Ed.*, 2018, **57**, 1261–1265.

273 Z.-J. Wang, J. Dong, Y. Cui, G. Eres, O. Timpe, Q. Fu, F. Ding, R. Schloegl and M.-G. Willinger, *Nat. Commun.*, 2016, **7**, 13256.